Supporting Information

Size-Dependent Dynamic Surface States of Ru Clusters: Modulating Interfacial Water Structure for Enhanced Alkaline Hydrogen Evolution Reaction

Jiwon Kim,[a†] Jinuk Moon,[b†] Kyuri Cho,[c†] Junhyeong Kim,[d†] Man Ho Han,[e] Seongbeen Kim,[a] Jimin Han,[b] Daeeun Choi,[a] Hyunwoo Jun,[a] Jong Hyun Jang,[d] Hyung-Suk Oh,[e] Sung Ki Cho,[*d] Wooyul Kim,[*c] Jeong Woo Han[*b] and Jinwoo Lee[*a]

[a]*Department of Chemical and Biomolecular Engineering, Korea Advanced Institute of Science and Technology (KAIST), Daejeon 34141, Republic of Korea.*

[b]*Department of Materials Science and Engineering, Research Institute of Advanced Materials, Seoul National University, Seoul 08826, Republic of Korea*

[c]*Department of Energy Engineering, Korea Institute of Energy Technology (KENTECH), Naju 58330, Republic of Korea.*

[d]*Hydrogen Fuel Cell Research Center, Korea Institute of Science and Technology (KIST), Seoul 02792, Republic of Korea*

[e]*Clean Energy Research Center, Korea Institute of Science and Technology (KIST), Seoul 02792, Republic of Korea*

† These authors contributed equally to this work.

*Corresponding authors: skcho@kist.re.kr, wkim@kentech.ac.kr, jwhan98@snu.ac.kr, jwlee1@kaist.ac.kr

Experimental Section

Materials

Ketjenblack EC-600JD was obtained from Mitsubishi Chemical. Ruthenium (III) chloride hydrate ($RuCl_3 \cdot xH_2O$, 99.9 %) and urea (99 %) were purchased from Sigma-Aldrich. Absolute ethanol was acquired from Fisher Scientific. Deionized (DI) water with a resistivity of 18.2 MΩ·cm was supplied by a Millipore purification system. Carbon paper (Sigracet 39BB) was sourced from Fuel Cell Store. D521 Nafion ionomer dispersion (alcohol-based, 1100 EW, 5 wt%) was purchased from DuPont. Isopropanol (IPA, 99.5 %) and 1.0 M KOH solution were obtained from Samchun Pure Chemical.

Catalyst synthesis

Preparation of Nitrogen-Doped Ketjenblack

Nitrogen-doped Ketjenblack (NKB) was synthesized via a urea-assisted soft nitriding strategy based on a previously reported method.[1] Briefly, 1.0 g of Ketjenblack EC-600JD and 1.5 g of urea were homogeneously mixed in an agate mortar to obtain a homogeneous mixture. The mixture was then transferred to an alumina crucible and thermally treated in air at 150 °C (ramp: 2 °C min^{-1}) for 2 h, followed by a second heating at 300 °C (ramp: 5 °C min^{-1}) for another 2 h. After cooling to room temperature, the resulting powder was dispersed in a 1:1 (v/v) ethanol/DI water mixture and stirred at 60 °C for 2 h. The suspension was then filtered and sequentially washed with ethanol and DI water. The collected powder was dried in a vacuum oven at 80 °C for 12 h.

Synthesis of Ru/NKB-T Catalysts

Ru on nitrogen-doped Ketjenblack (Ru/NKB) catalysts were synthesized via a wet-impregnation method followed by a controlled thermal reduction. 200 mg of NKB was dispersed in 20 mL of ethanol under vigorous stirring, followed by the dropwise addition of a $RuCl_3 \cdot xH_2O$ solution (5 wt% in DI water). After sonication, the suspension was dried at 50 °C under stirring and further dried in a vacuum oven at 50 °C for 12 h. The dried powder was then transferred to an alumina crucible and reduced in a flowing 10 % H_2/Ar atmosphere. The samples were annealed at target temperatures (200, 350, 500, 650, and 800 °C) with a ramping rate of 1 °C min^{-1} and maintained for 2 h. The final catalysts were denoted as Ru/NKB-T, where T represents the annealing temperature.

Characterizations

High-angle annular dark-field scanning transmission electron microscopy (HAADF-STEM) and energy-dispersive X-ray spectroscopy (EDS) mapping were acquired using a double Cs-corrected transmission electron microscope (Spectra Ultra, Thermo Fisher Scientific). X-ray diffraction (XRD) patterns were collected using an X-ray diffractometer (SmartLab, Rigaku) equipped with Cu Kα radiation (λ = 1.541 Å). Elemental analysis of C, H, N, and S was conducted using a FlashSmart elemental analyzer (Thermo Fisher Scientific), while the oxygen content was determined with a Flash 2000 series elemental analyzer (Thermo Scientific). X-ray photoelectron spectroscopy (XPS) measurements were carried out using an Axis Supra spectrometer (Kratos) with Al Kα radiation. Inductively coupled plasma mass spectrometry (ICP-MS) analysis was performed using an ICP-MS 7700S (Agilent). X-ray absorption spectroscopy (XAS) at the Ru K-edge was conducted at the 8C Nano XAFS and 10C Wide XAFS beamlines of the Pohang Accelerator Laboratory (PAL), Korea. Spectra were collected in both transmission and fluorescence modes. A Ru foil reference was measured simultaneously for energy calibration. Data processing, including background subtraction and normalization, and linear combination fitting (LCF) were performed using Athena, while Fourier-transformed k^2-weighted X-ray absorption fine structure (FT-EXAFS) fitting was carried out using Artemis within the Demeter software package. The amplitude reduction factor (S_o^2) was obtained from Ru foil fitting. Wavelet transform EXAFS (WT-EXAFS) analyses were performed using the Morlet wavelet with $\eta \cdot \sigma$ values of 10 for overview maps and 36 for detailed analysis.[2]

Electrochemical measurements

Electrochemical measurements were performed at a Reference 600 potentiostat (Gamry Instruments) in a standard three-electrode system. A rotating disk electrode (RDE) with a glassy carbon disk (diameter: 5 mm) was used as the working electrode, while a graphite rod and an Hg/HgO electrode (in 1.0 M NaOH) were used as the counter and reference electrodes, respectively. The reference electrode was calibrated in H_2-saturated 1.0 M KOH using Pt wires as both working and counter electrodes, yielding a potential offset of - 0.928 V versus the reversible hydrogen electrode (RHE). To prepare the catalyst ink, 2.7 mg of the synthesized catalyst was dispersed in a mixture of 380 μL DI water, 600 μL isopropanol, and 20 μL Nafion ionomer solution (D521) and sonicated for 2 h. A 12 μL aliquot of the ink was drop-cast onto the rotating disk electrode (RDE) surface three times, resulting in a total catalyst loading of approximately 0.5 mg cm^{-2}. For comparison, commercial 20 wt% Pt/C (HISPEC 3000, Johnson

Matthey) and 20 wt% Ru/C (Premetek) catalysts were deposited onto the RDE to achieve a noble-metal loading of 15 μg_{NM} cm^{-2}, identical to that of Ru/NKB-500. In addition, Pt/C with a higher noble-metal loading of 42 μg_{NM} cm^{-2} (corresponding to its nominal loading) was also evaluated.[3]

All electrochemical measurements were conducted in H_2-saturated 1.0 M KOH electrolyte after purging with H_2 for at least 10 min. Linear sweep voltammetry (LSV) was performed at a rotation speed of 1,600 rpm with a scan rate of 1 mV s^{-1}, and iR compensation was applied. Electrochemical impedance spectroscopy (EIS) measurements were carried out over a frequency range from 100 kHz to 100 mHz with a perturbation amplitude of 5 mV at - 30 mV vs. RHE. To minimize capacitive current contributions, Tafel slopes were derived from multi-step chronopotentiometry by holding each current step for 20 s with logarithmic current density intervals of 0.05 in log[j (mA cm^{-2})]. Stability tests were evaluated by chronopotentiometry at a constant current density of - 20 mA cm^{-2} for 86,400 s.

Calculation of Electrochemical Surface Area

Electrochemical Surface Area **(**ECSA) was estimated by evaluating the electrochemical double-layer capacitance (C_{dl}) of the catalysts. Cyclic voltammetry (CV) was performed in H_2-saturated 1.0 M KOH within a non-Faradaic potential window of 0.3-0.4 V vs. RHE at scan rates of 20, 40, 60, 80, and 100 mV s^{-1}. For each scan rate, five consecutive CV cycles were recorded, and the current density values from the final cycle were used. The capacitive current density ($\Delta j/2$) at 0.35 V vs. RHE was determined as $(j_{anodic} - j_{cathodic})/2$, and C_{dl} was obtained from the slope of the linear fit of $\Delta j/2$ versus scan rate. The ECSA was calculated using the following equation:

$$ECSA = \frac{Cdl}{Cs} S$$

where Cs is the specific capacitance of a smooth planar surface, which is typically considered in the range of 20-60 μF cm^{-2}. In this work, Cs=40 μF cm^{-2} was adopted. All samples were evaluated under identical conditions, allowing a consistent comparison of relative ECSA values. The real surface area S was assumed to be equivalent to the geometric area of the glassy carbon electrode (S = 0.19635 cm^2).

AEMWE electrode fabrication and single-cell measurements

The electrodes for anion exchange membrane water electrolysis (AEMWE) were fabricated by spray-coating catalyst inks onto substrates. For the cathode, Ru/NKB-T catalyst powder was

dispersed in DI water and subsequently mixed with an anion exchange ionomer and isopropyl alcohol, with an ionomer-to-catalyst (I/C) ratio of 0.1. The obtained catalyst ink was hand-sprayed onto a gas diffusion layer (Sigracet 39BB, thickness: 315 μm) with an exposed active area of 1.0 cm^2. For comparison, the commercial PtRu/C (Sigma-Aldrich, 738573) and Pt/C (Tanaka K.K., 37.3 wt%) -based cathodes were also prepared using the same procedure. The loading amount of noble metal (NM) for the cathode was fixed at approximately 0.15 mg cm^{-2}. For the anode, a home-made NiFe alloy catalyst was used to fabricate the anode for AEMWE.[4] The anode catalyst was spray-coated onto Ni felt (Bekaert, 2Ni18-025, thickness: 250 μm) with a catalyst loading of 2.0 mg cm^{-2}.

For the AEMWE single cell configuration, the anion exchange membrane (Dioxide materials, X37-50 Grade RT, thickness: 50 μm) was positioned between the as-prepared cathode and anode to assemble the zero-gap MEA. The gasket thicknesses for the cathode and anode sides were 250 μm and 230 μm, respectively. Prior to AEMWE operation, the cell temperature was raised to 50 °C and preheated 1.0 M KOH electrolyte was supplied to both the cathode and anode sides at a flow rate of 20 mL min^{-1}. To evaluate high-temperature performance and long-term durability, additional AEMWE operation was conducted using a PiperION anion exchange membrane (Versogen, thickness: 20 μm). Chronopotentiometry was employed to assess the operational stability of the AEMWE cell at a constant current density of 1.0 A cm^{-2} for 400 h, while all other operating conditions were kept identical.

In situ XAS measurement

In situ XAS experiments were conducted at the 10C Wide XAFS beamline at PAL using a custom-designed three-electrode electrochemical cell. The working electrode was fabricated by spray-coating the catalyst ink onto carbon paper (Sigracet 39BB) to achieve a Ru loading of 0.15 mg_{NM} cm^{-2}. The catalyst ink was prepared by dispersing 30 mg of the Ru/NKB-T catalyst in a mixture of 300 μL DI water, 1500 μL isopropanol, and 130 μL Nafion solution. A graphite rod and an Hg/HgO electrode were employed as the counter and reference electrodes, respectively. During the measurements, 1.0 M KOH electrolyte was continuously circulated at a flow rate of 0.1 mL min^{-1}. XAS spectra were collected in both transmission and fluorescence modes under chronoamperometric conditions. Each applied potential was held for at least 10 min to ensure steady-state conditions before data acquisition.

In situ ATR-SEIRAS measurement

In situ attenuated total reflection surface-enhanced infrared absorption spectroscopy (ATR-SEIRAS) measurements were conducted. An Au-coated Si prism (PIKE, 60º of the incident angle and 2 cm in diameter) was used due to its excellent compatibility with uniform metal film deposition and strong plasmonic enhancement for SEIRAS signals. The Au thin film, serving as the SEIRAS active layer, was prepared on the Si substrate by electroless plating.[5] After coating gold, catalyst ink was spray-coated onto the Au-coated surface. The catalyst ink was prepared by mixing 100 μL of a 1 wt% catalyst dispersion (prepared in DI water), 50 μL of isopropyl alcohol, and 2 μL of Nafion 117 solution (5 wt% mixture in alcohol and water, Sigma-Aldrich). The prepared substrate was then mounted in a Pyrex reactor for SEIRAS measurements.

The SEIRAS cell was connected to a VERTEX 80v FT-IR spectrometer (Bruker) equipped with an MCT detector and a variable-angle ATR accessory (Veemax III, Pike Technologies). Spectra were collected in absorbance mode at a resolution of 4 cm^{-1}.

Electrochemical measurements were performed using the Au-coated substrate as the working electrode, Ag/AgCl as the reference electrode, and a Pt wire as the counter electrode in Ar-purged 1.0 M KOH. Stepwise chronoamperometry was conducted by holding potentials from 0 V to - 0.3 V (vs. RHE) in 0.05 V increments.

DFT calculations

Density functional theory (DFT) calculations were performed using the Vienna Ab initio Simulation Package (VASP).[6, 7] The Perdew-Burke-Ernzerhof (PBE) exchange-correlation functional within the generalized gradient approximation (GGA) was employed together with projector augmented wave (PAW) pseudopotentials.[8, 9] A plane-wave kinetic energy cutoff of 450 eV was applied for all calculations. Electronic self-consistency was converged to 1 x 10^{-5} eV, and ionic relaxations proceeded until residual forces fell below 0.05 eV/Å. All calculations were spin-polarized, and reciprocal space was sampled at the Gamma point for all cluster and single-atom models. Bader charge analysis was performed to quantify charge redistribution between Ru and the carbon support.

Three computational models were constructed to represent the size-dependent atomic structures of Ru catalysts. For the atomically dispersed Ru/NKB-200, a single Ru atom coordinated with three nitrogen atoms (Ru-N_3) was embedded in a graphene substrate. For the sub-nanometer Ru/NKB-500 and the larger nanocluster Ru/NKB-800, icosahedral Ru_{55} and Ru_{147} cluster models were adopted, respectively, to capture the experimentally observed size difference. Gibbs free energies (G) were obtained by correcting DFT total energies (E) with

the zero-point energy (ZPE) and entropic contributions (S) at T = 298.15 K according to $\Delta G = E + \Delta ZPE - T\Delta S$.

The computational hydrogen electrode (CHE) model was applied to describe the thermodynamics of proton-electron transfer steps, where the chemical potential of a proton-electron pair ($H^+ + e^-$) is referenced to one-half the chemical potential of gaseous H_2 at standard conditions.[10]

Molecular dynamics simulations of interfacial water structure

Molecular dynamics (MD) simulations based on the NequIP-OAM-XL pretrained machine-learning interatomic potential (MLIP) were carried out to investigate the hydrogen-bond network of interfacial water on Ru surfaces with different atomic configurations.[11, 12] Simulation cells were constructed by placing a 20 Å layer of explicit water molecules on the respective Ru surface models, with a 10 Å vacuum region along the surface-normal direction to prevent periodic image interactions. All MD simulations were performed in the NVT ensemble at 300 K using a Langevin thermostat. Production trajectories were extended to 1 ns for each system, and five independent runs per sample were carried out to ensure statistical reliability.

Hydrogen-bond analysis was performed using the HydrogenBondAnalysis module implemented in MDAnalysis.[13] A hydrogen bond was identified when the O···O distance between the donor and acceptor was 3.5 Å or less and the O-H···O angle was 140 degrees or greater.

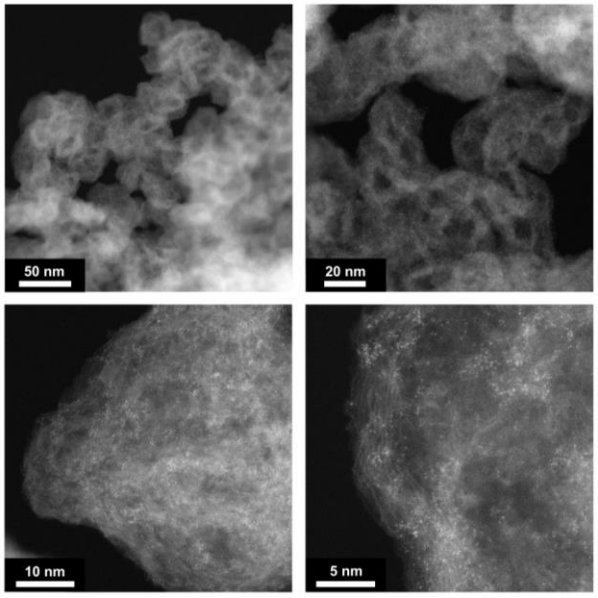

Fig. S1 Representative HAADF-STEM images of Ru/NKB-200 at different magnifications.

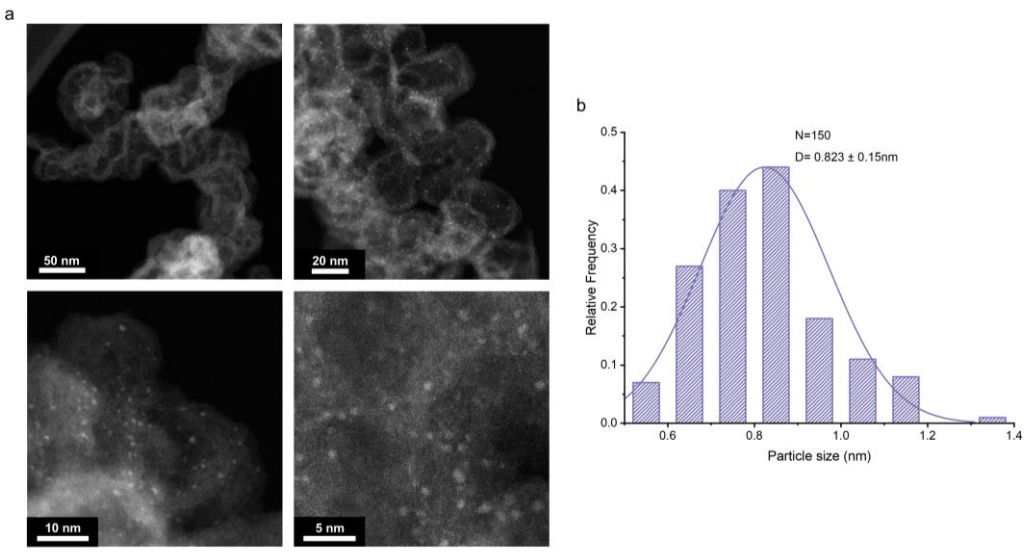

Fig. S2 HAADF-STEM characterization of Ru/NKB-350. (a) Representative HAADF-STEM images of Ru/NKB-350 at different magnifications. (b) Corresponding particle size distribution histogram.

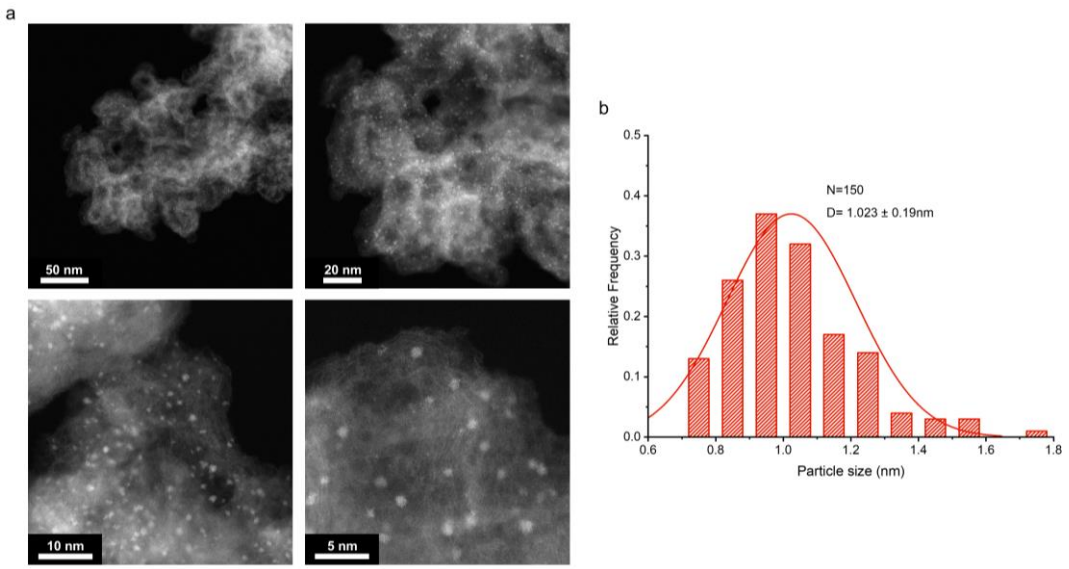

Fig. S3 HAADF-STEM characterization of Ru/NKB-500. (a) Representative HAADF-STEM images of Ru/NKB-500 at different magnifications. (b) Corresponding particle size distribution histogram.

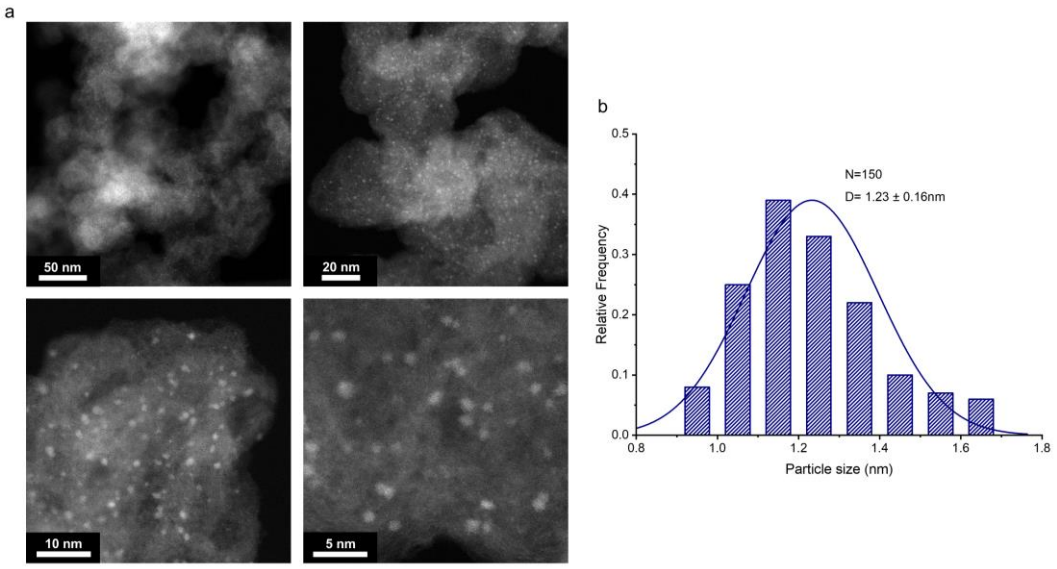

Fig. S4 HAADF-STEM characterization of Ru/NKB-650. (a) Representative HAADF-STEM images of Ru/NKB-650 at different magnifications. (b) Corresponding particle size distribution histogram.

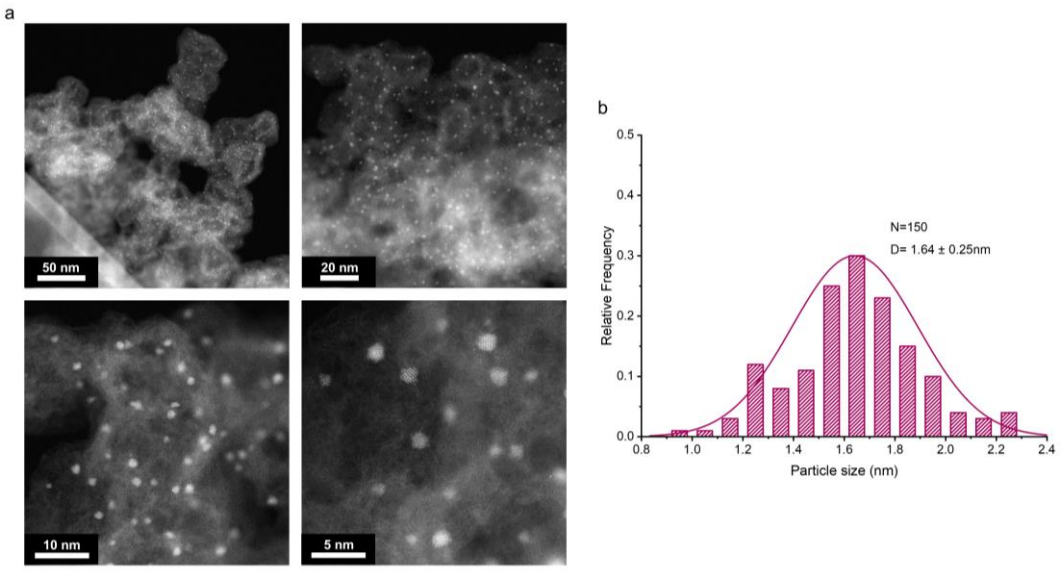

Fig. S5 HAADF-STEM characterization of Ru/NKB-800. (a) Representative HAADF-STEM images of Ru/NKB-800 at different magnifications. (b) Corresponding particle size distribution histogram.

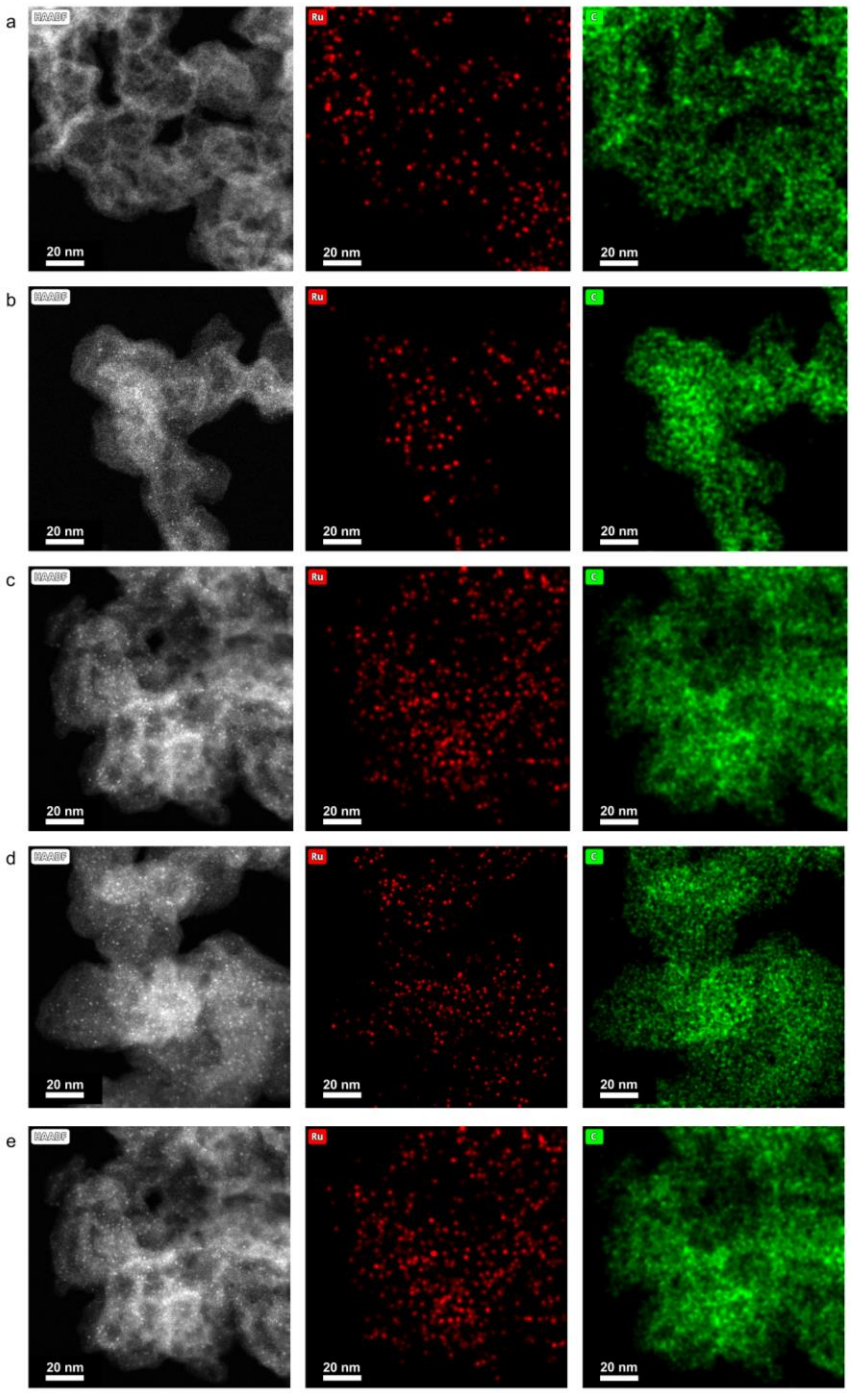

Fig. S6 HAADF-STEM images and corresponding EDS elemental mapping of Ru/NKB-T catalysts. Representative images and elemental mapping of (a) Ru/NKB-200, (b) Ru/NKB-350, (c) Ru/NKB-500, (d) Ru/NKB-650, and (e) Ru/NKB-800 (red: Ru, green: C).

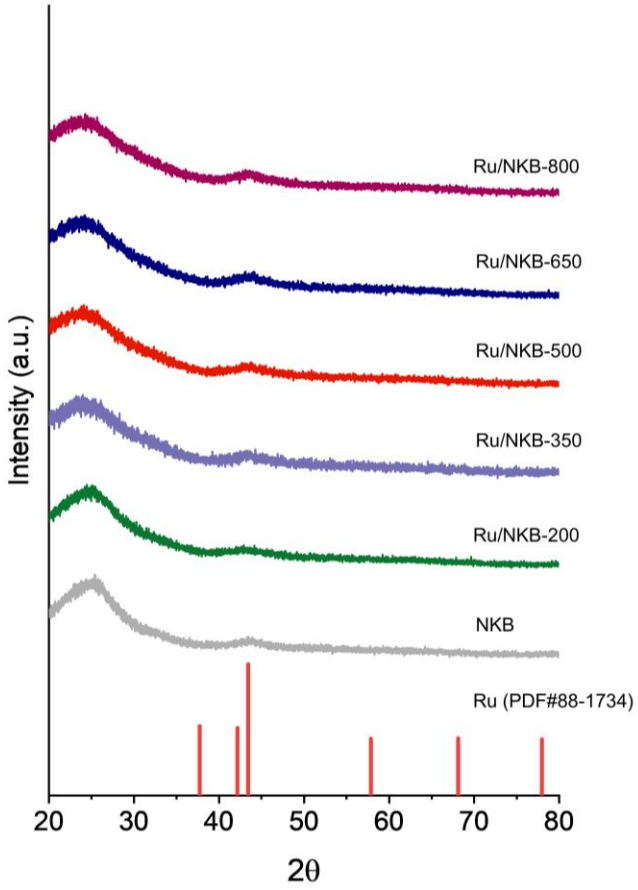

Fig. S7 XRD patterns of NKB and Ru/NKB-T (T = 200, 350, 500, 650, and 800 ℃), with the reference diffraction peaks of metallic Ru (PDF#88-1734) indicated.

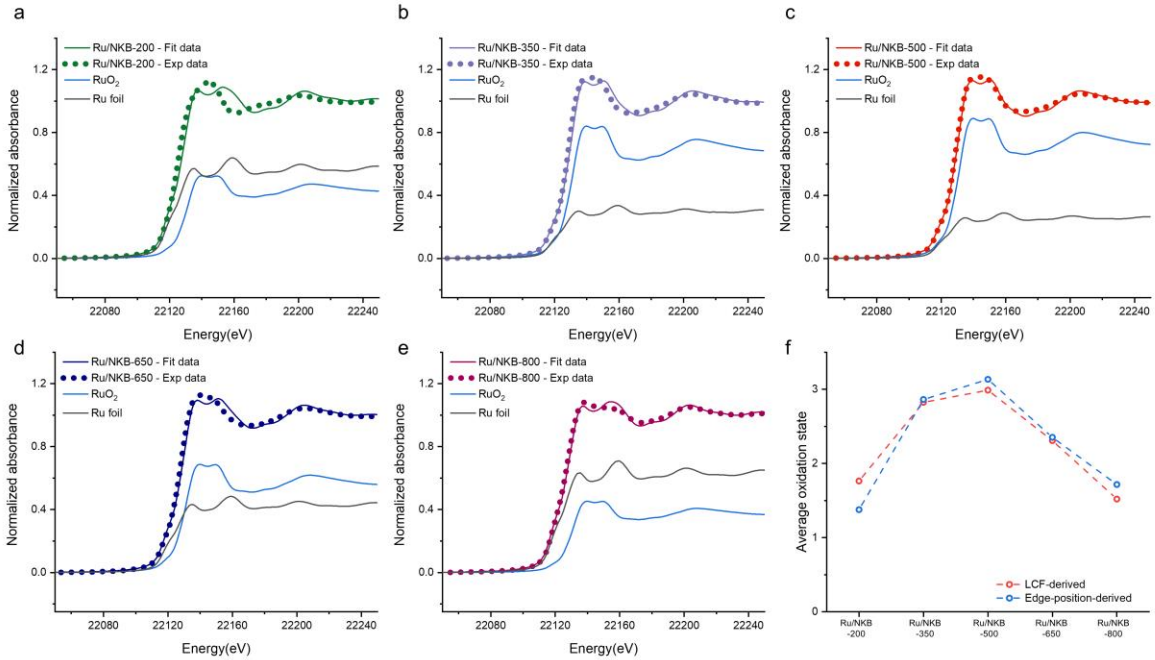

Fig. S8 LCF analysis of Ru K-edge XANES spectra for the Ru/NKB-T catalysts. Experimental Ru K-edge XANES spectra and corresponding LCF results obtained using Ru foil and RuO_2 as reference spectra for (a) Ru/NKB-200, (b) Ru/NKB-350, (c) Ru/NKB-500, (d) Ru/NKB-650, and (e) Ru/NKB-800. Dotted and solid lines represent the experimental spectra and LCF fits, respectively. (f) Comparison of the average Ru oxidation states derived from edge position and LCF. Note: The distinct coordination environment of the atomically dispersed Ru/NKB-200 cannot be fully represented by the bulk Ru foil and RuO_2 reference spectra.[14] Nevertheless, the LCF result was used as a relative spectral descriptor for comparing the oxidized Ru contribution across the Ru/NKB-T series.

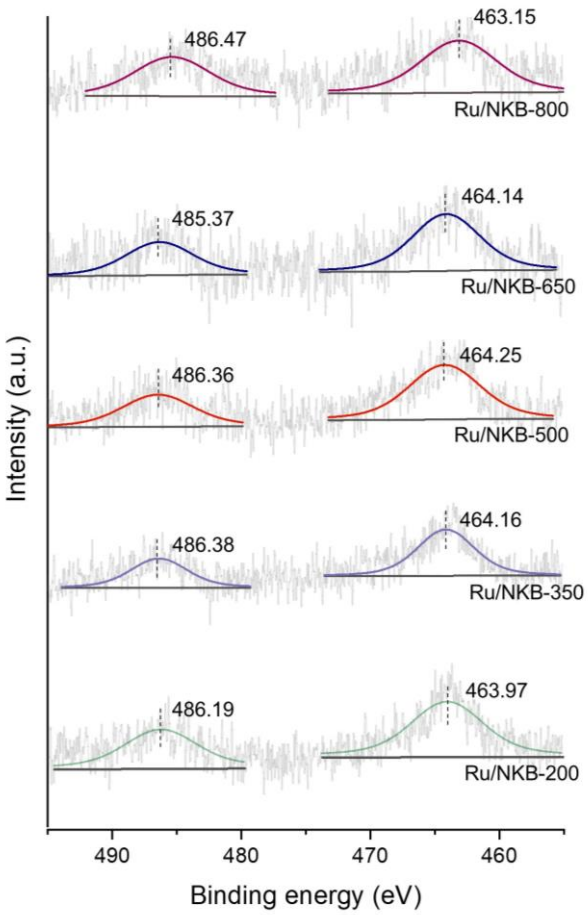

Fig. S9 Ru 3p XPS spectra of Ru/NKB-T catalysts (T = 200, 350, 500, 650, 800 °C).

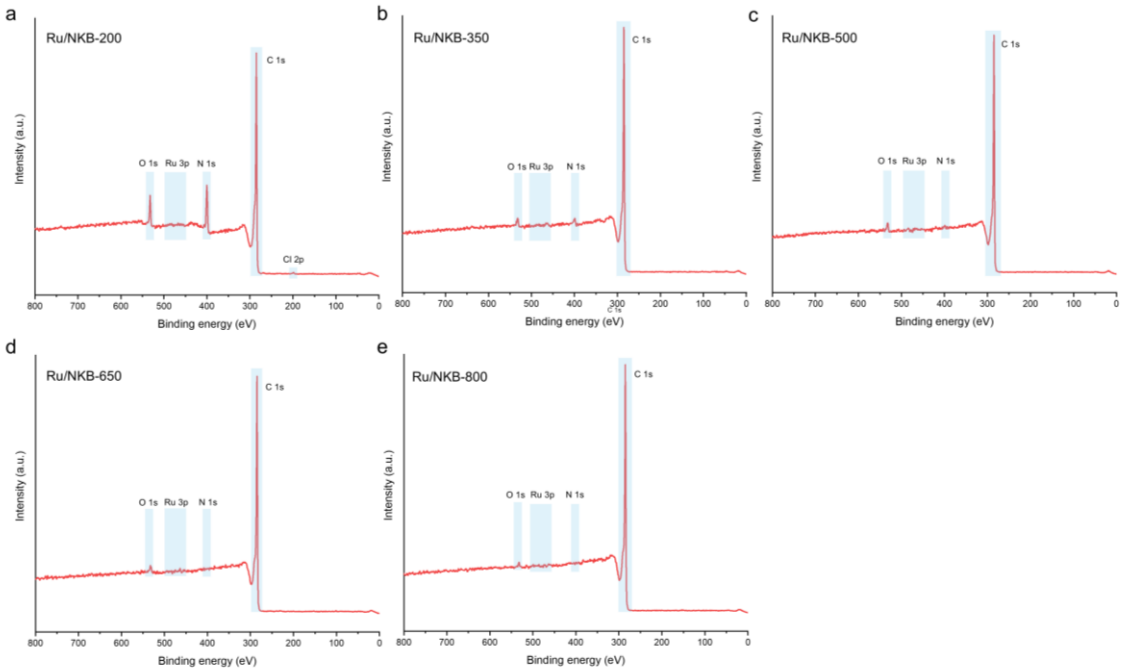

Fig. S10 XPS survey spectra of Ru/NKB-T catalysts. (a) Ru/NKB-200, (b) Ru/NKB-350, (c) Ru/NKB-500, (d) Ru/NKB-650, and (e) Ru/NKB-800.

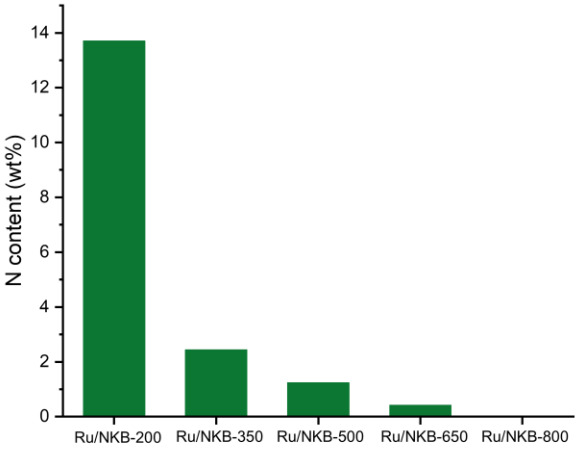

Fig. S11 Nitrogen content of Ru/NKB-T catalysts determined by CHNS elemental analysis (T = 200, 350, 500, 650, and 800 ℃).

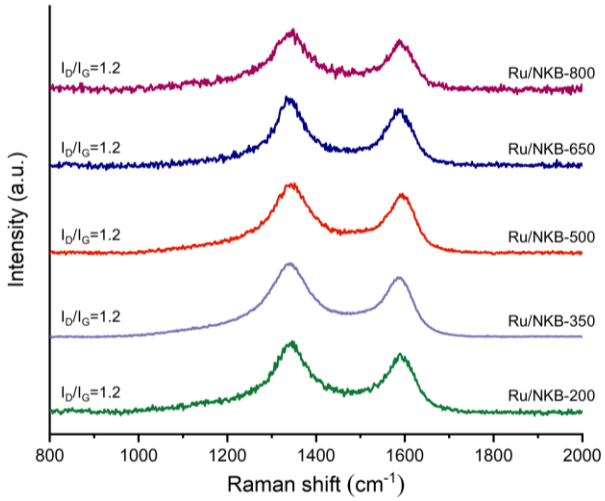

Fig. S12 Raman spectra of Ru/NKB-T catalysts (T = 200, 350, 500, 650, and 800 ℃).

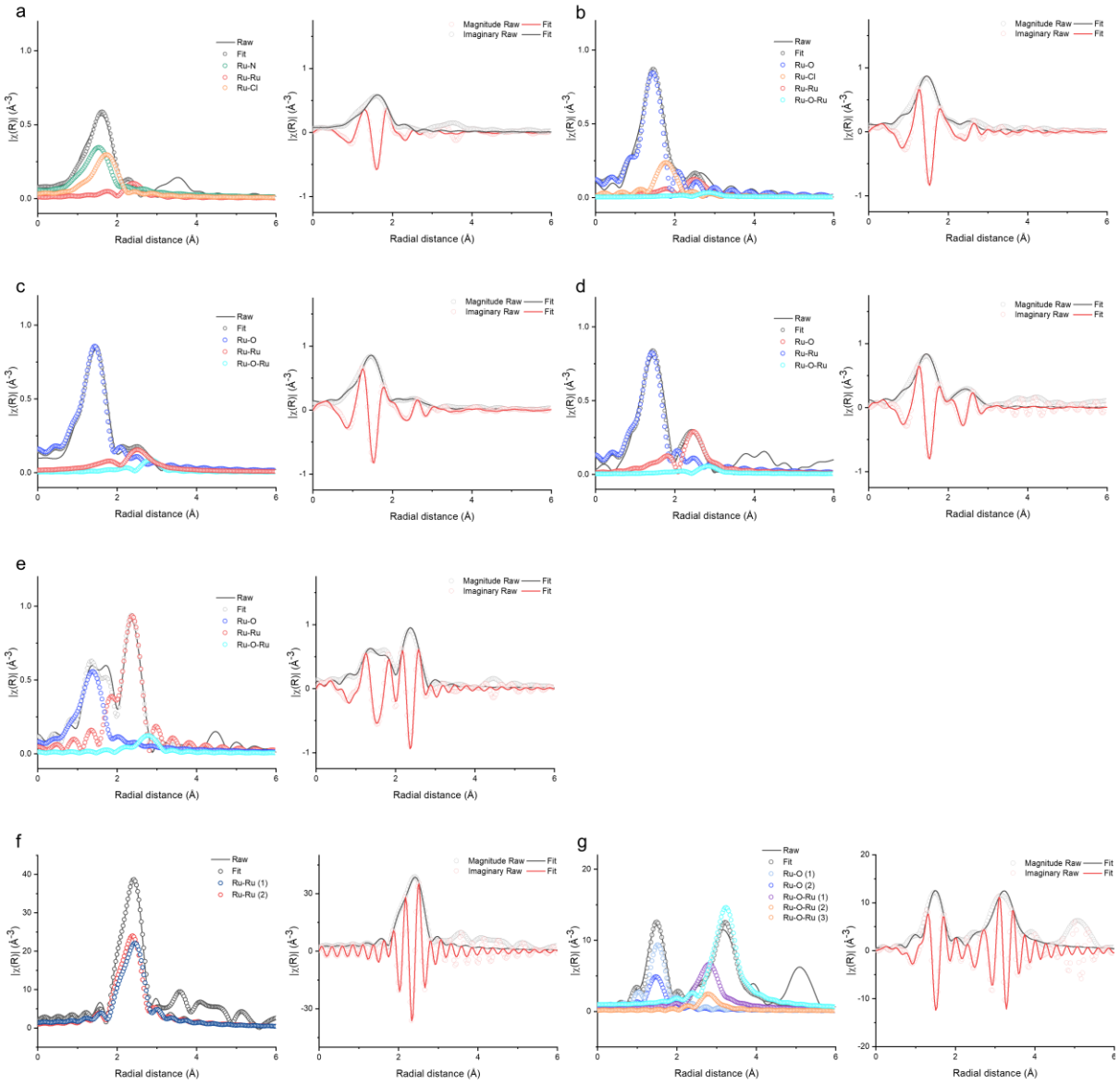

Fig. S13 Ru K-edge EXAFS experimental data and fitting results in R-space. The left panels show the experimental EXAFS magnitude and individual scattering paths used for fitting, whereas the right panels present the corresponding R-space fits including magnitude and imaginary components for (a) Ru/NKB-200, (b) Ru/NKB-350, (c) Ru/NKB-500, (d) Ru/NKB-650, (e) Ru/NKB-800, (f) Ru foil, and (g) RuO_2.

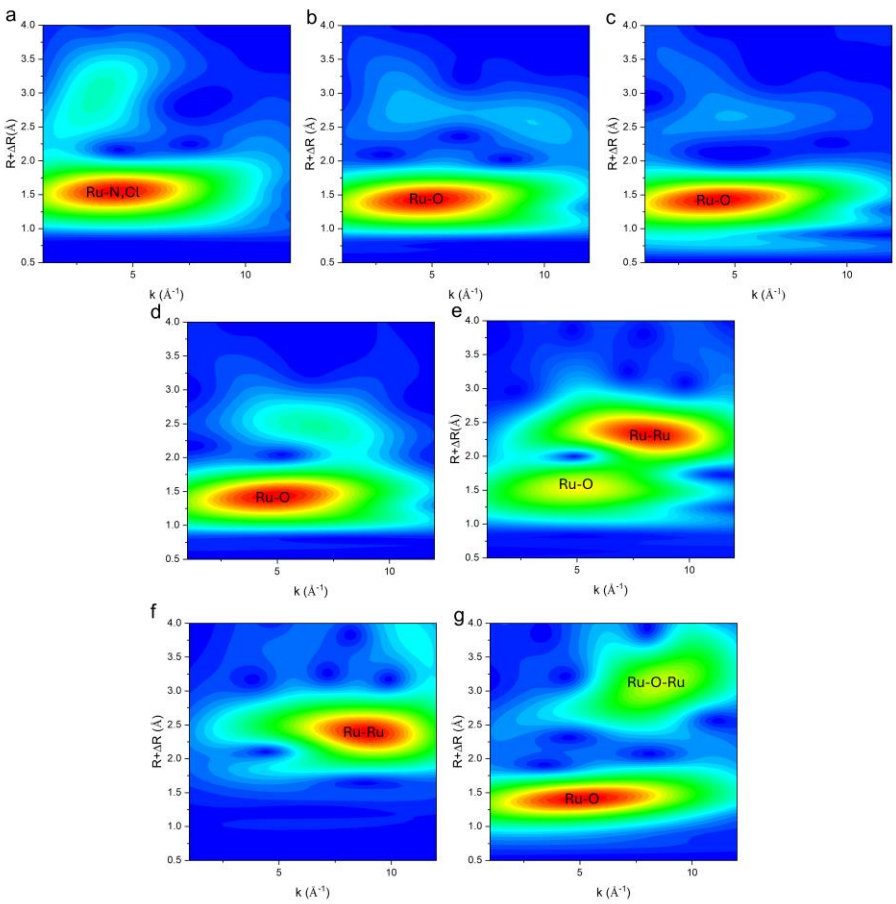

Fig. S14 Ru K-edge WT-EXAFS contour plots. The plots display the k^2-weighted $\chi(k)$ signals for (a) Ru/NKB-200, (b) Ru/NKB-350, (c) Ru/NKB-500, (d) Ru/NKB-650, (e) Ru/NKB-800, (f) Ru foil, and (g) RuO_2.

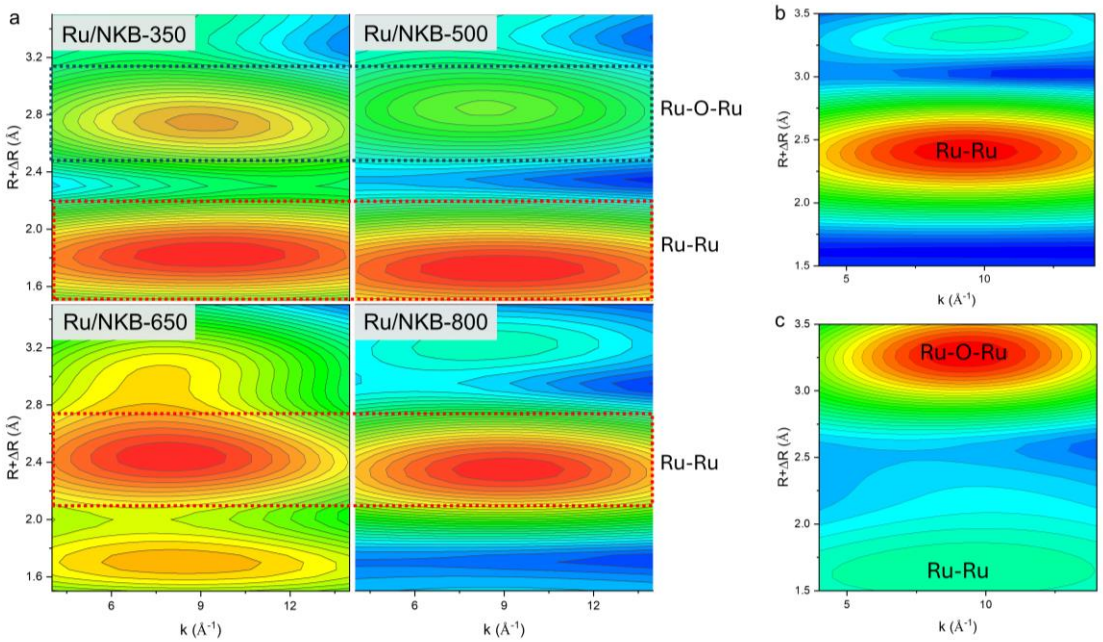

Fig. S15 Detailed Ru K-edge WT-EXAFS contour plots for the second coordination shell to distinguish Ru-O-Ru and Ru-Ru scattering paths. (a) Ru/NKB-T catalysts (T = 350, 500, 650, and 800 ℃), (b) Ru foil, and (c) RuO_2.

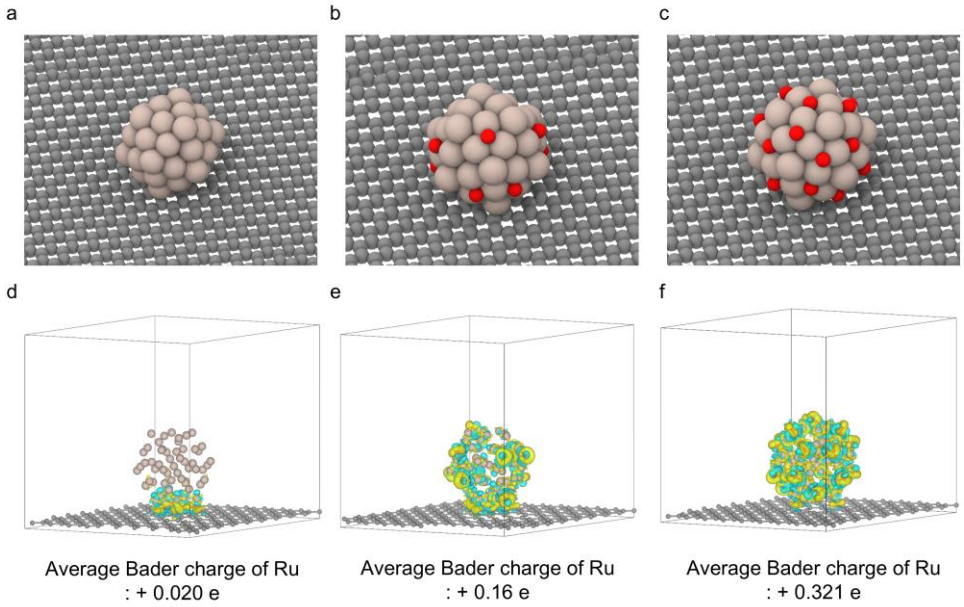

Fig. S16 Atomic models and charge density distributions of Ru_{55}-based Ru/NKB-500 models with different degrees of surface oxidation. Atomic structures of carbon-supported (a) metallic Ru_{55} and oxidized Ru_{55} models with (b) lower oxygen coverage and (c) higher oxygen coverage. Corresponding charge density distributions and average Bader charges of Ru for (d) metallic Ru_{55} and oxidized Ru_{55} models with (e) lower oxygen coverage and (f) higher oxygen coverage.

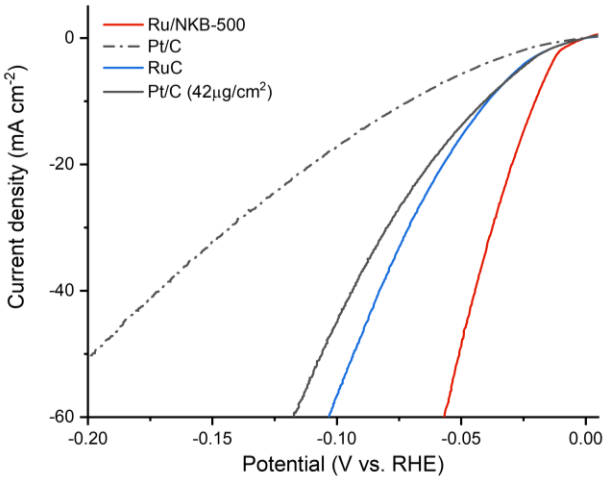

Fig. S17 LSV polarization curves for the alkaline hydrogen evolution reaction (HER) measured on Ru/NKB-500, Pt/C, and Ru/C at the same metal loading (15 μg cm^{-2}). For comparison, Pt/C was also evaluated at a higher nominal loading (42 μg cm^{-2}).

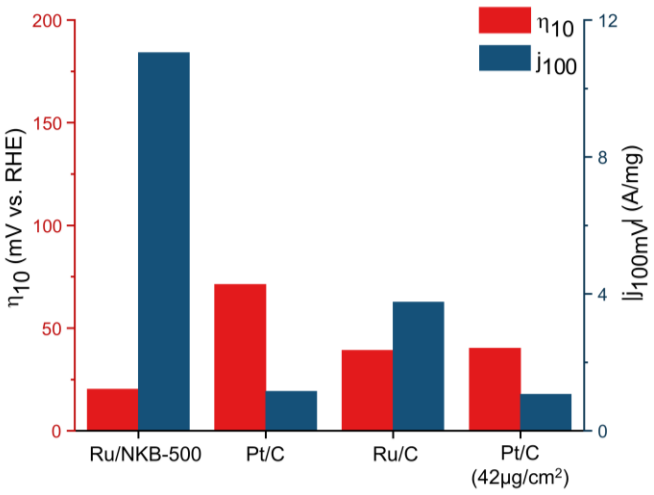

Fig. S18 Comparison of the overpotentials required to reach a current density of 10 mA cm^{-2} and the mass activities calculated at - 100 mV (vs. RHE) for Ru/NKB-500, Pt/C (15 μg cm^{-2} and 42 μg cm^{-2}), and Ru/C catalysts.

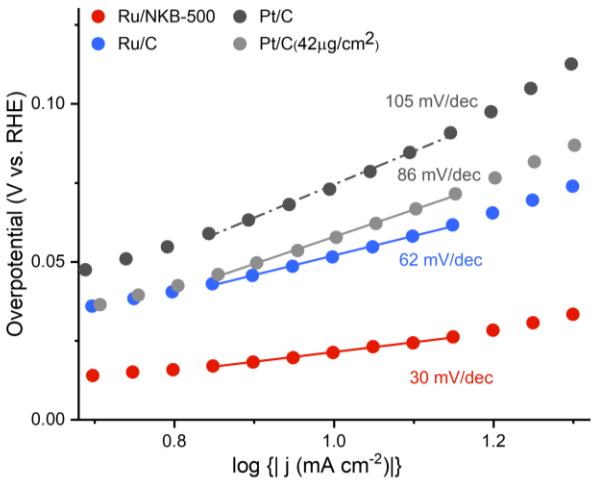

Fig. S19 Tafel plots measured for Ru/NKB-500, Pt/C (15 μg cm^{-2} and 42 μg cm^{-2}), and Ru/C catalysts.

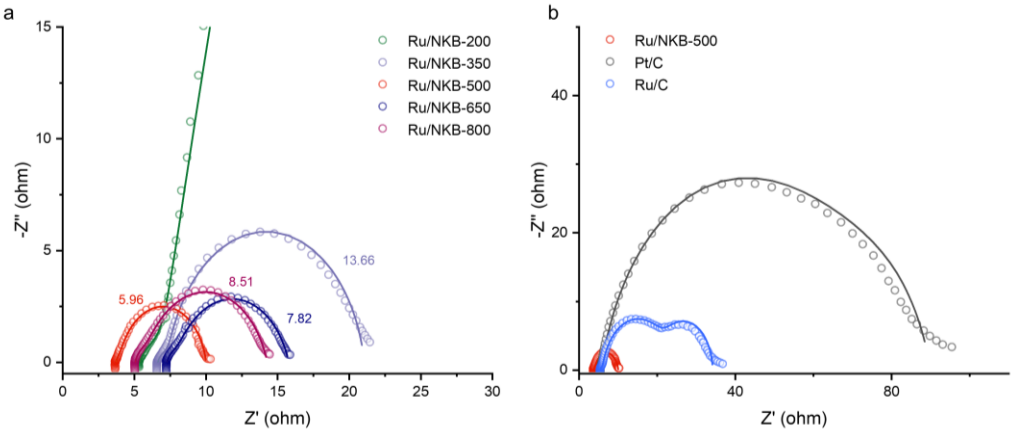

Fig. S20 EIS Nyquist plots measured at - 30 mV vs. RHE in H_2-saturated 1.0 M KOH. (a) Ru/NKB-T catalysts (T = 200, 350, 500, 650, and 800 ℃). (b) Ru/NKB-500 compared with Pt/C and Ru/C.

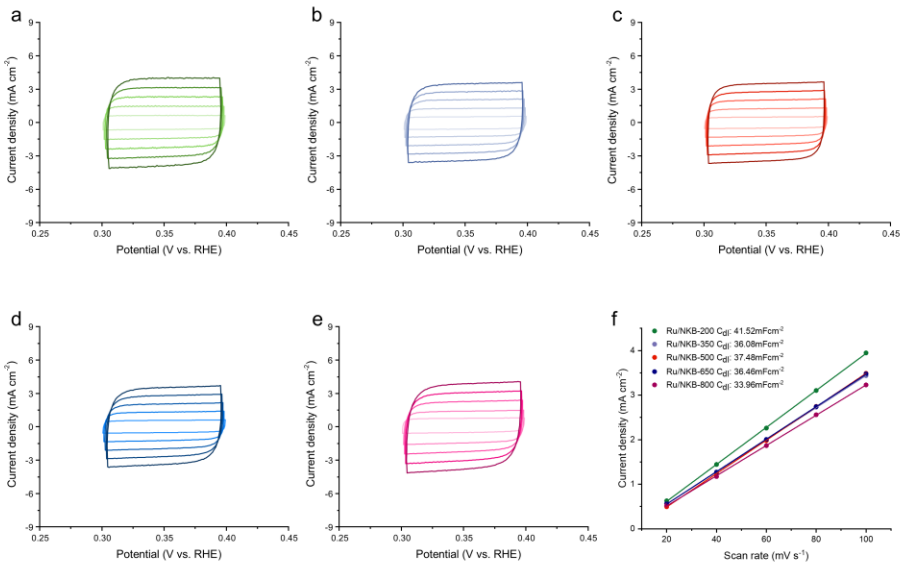

Fig. S21 CV curves and double-layer capacitance analysis. CV curves recorded at scan rates of 20, 40, 60, 80, and 100 mV s^{-1} for (a) Ru/NKB-200, (b) Ru/NKB-350, (c) Ru/NKB-500, (d) Ru/NKB-650, and (e) Ru/NKB-800. (f) Linear fitting of the capacitive current as a function of scan rate and the corresponding C_{dl} values.

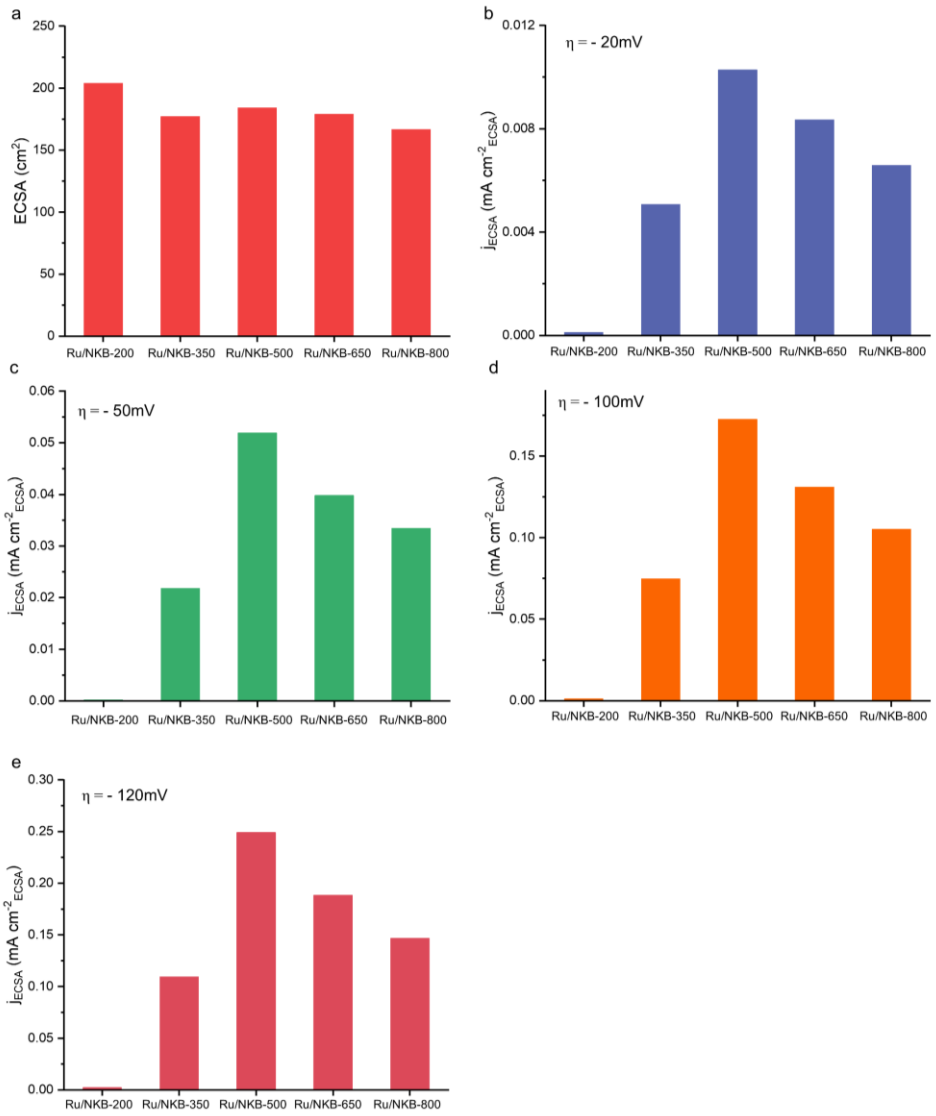

Fig. S22 Calculated ECSA and ECSA-normalized current densities. (a) ECSA values and ECSA-normalized current densities at overpotentials of (b) - 20 mV, (c) - 50 mV, (d) - 100 mV, and (e) - 120 mV for Ru/NKB-T catalysts (T = 200, 350, 500, 650, and 800 ℃).

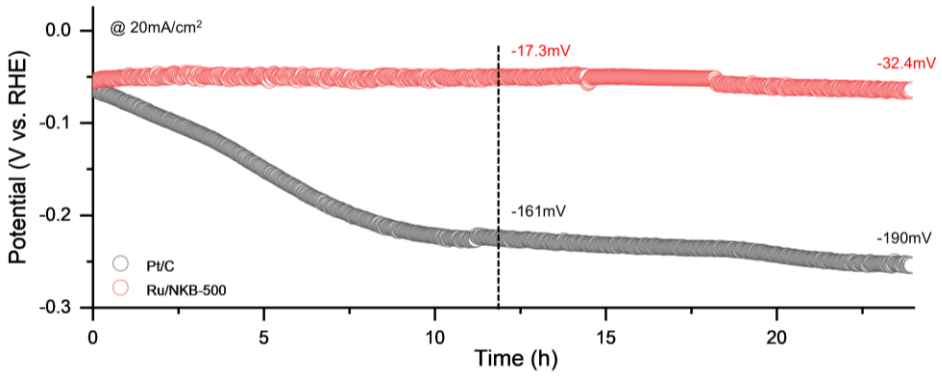

Fig. S23 Chronopotentiometric stability test of Ru/NKB-500 and Pt/C for the alkaline HER at a current density of - 20 mA cm^{-2}.

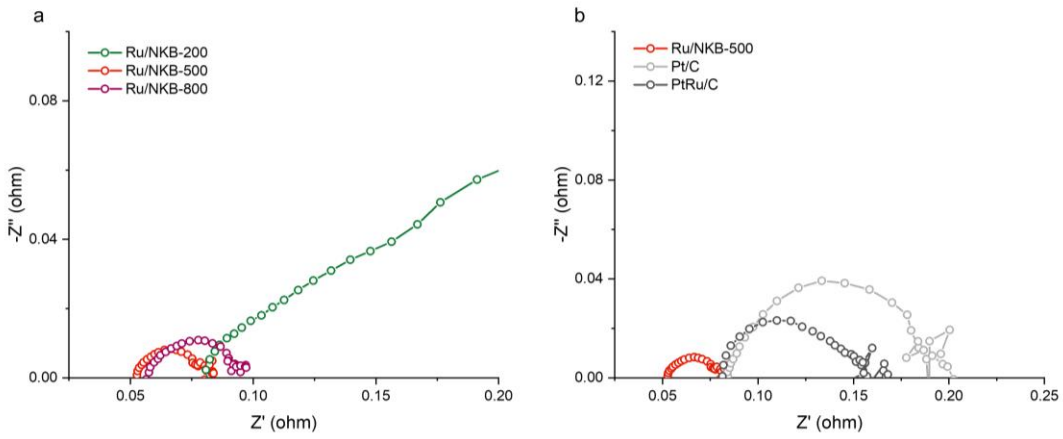

Fig. S24 EIS Nyquist plots of AEMWE cells recorded at a cell voltage of 1.8 V. (a) Comparison of Ru/NKB-T cathodes (T = 200, 500, and 800 °C) and (b) Comparison of Ru/NKB-500 with commercial Pt/C and PtRu/C benchmarks.

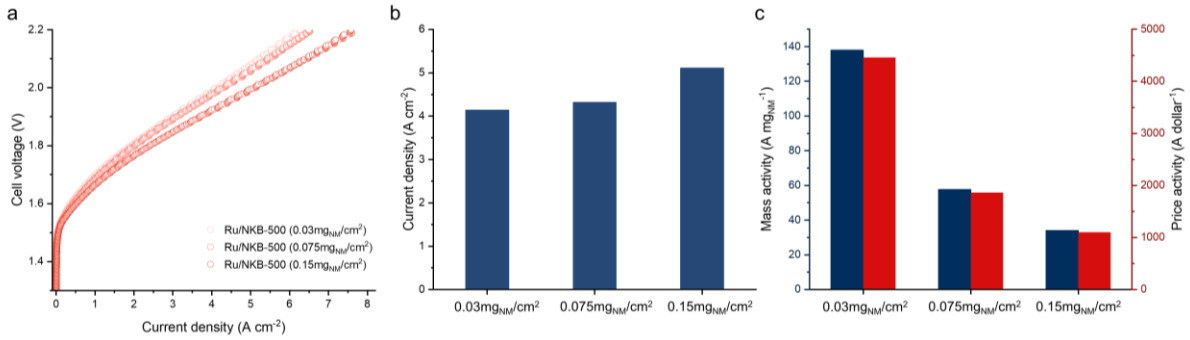

Fig. S25 Performance evaluation of AEMWE cells employing Ru/NKB-500 cathodes at 50 °C. (a) Polarization curves measured with different NM loadings (0.03, 0.075, and 0.15 mg_{NM} cm^{-2}) and temperature 50 ℃. (b) Current densities at a cell voltage of 2.0 V as a function of NM loading. (c) Corresponding mass activities and price activities calculated at 2.0 V.

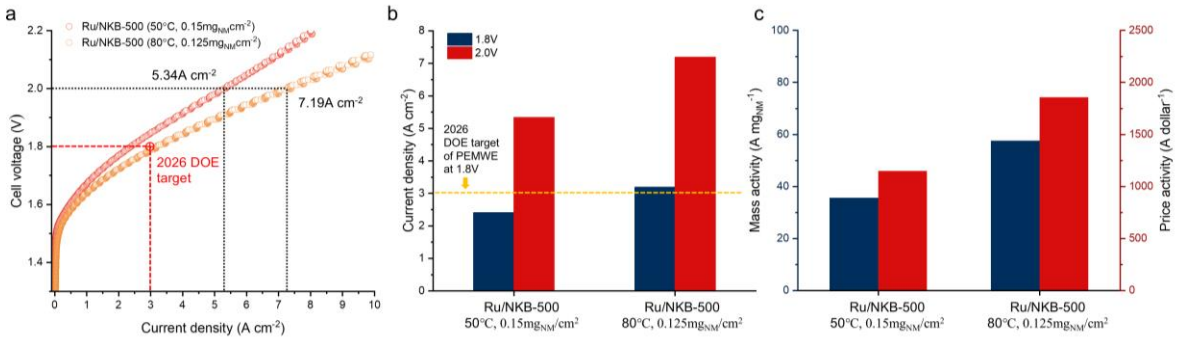

Fig. S26 Performance comparison of AEMWE cells employing Ru/NKB-500 cathodes at 80 °C with 0.125 mg_{NM} cm^{-2}. (a) Polarization curves measured with different NM loadings and temperatures (50 °C and 0.15 mg_{NM} cm^{-2}, 80 °C and 0.125 mg_{NM} cm^{-2}). (b) Current densities at a cell voltage of 1.8 V and 2.0 V. (c) Corresponding mass activities and price activities calculated at 2.0 V.

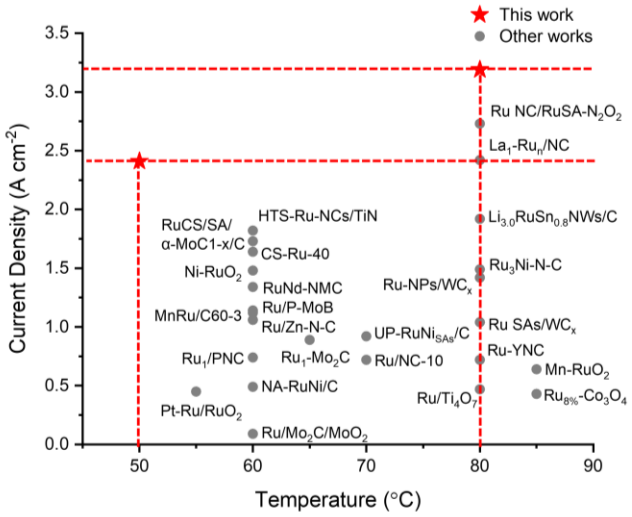

Fig. S27 Current densities at 1.8 V collected from previously reported AEMWE systems operated at low temperatures (50-90 °C). Each data point is labeled with the corresponding catalyst and reference. The red star denotes the performance achieved in this work. Literature references are listed in Table S5.

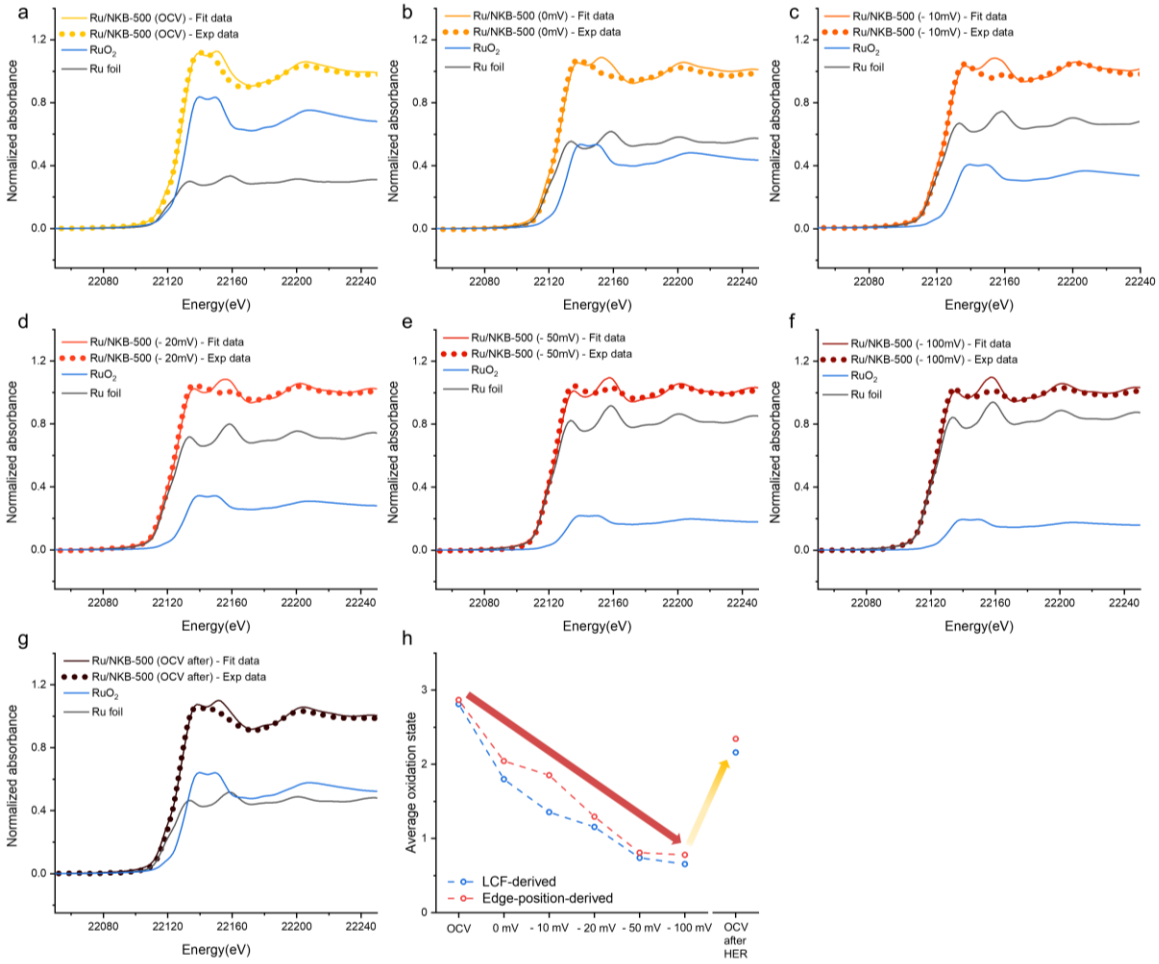

Fig. S28 LCF analysis of in situ Ru K-edge XANES spectra for Ru/NKB-500. Experimental Ru K-edge XANES spectra and corresponding LCF results obtained using Ru foil and RuO_2 as reference spectra for Ru/NKB-500 measured at (a) OCV, (b) 0 mV, (c) - 10 mV, (d) - 20 mV, (e) - 50 mV, (f) - 100 mV, and (g) OCV after HER. Dotted and solid lines represent the experimental spectra and LCF fits, respectively. (h) Comparison of the average Ru oxidation states derived from edge position and LCF under applied HER potentials.

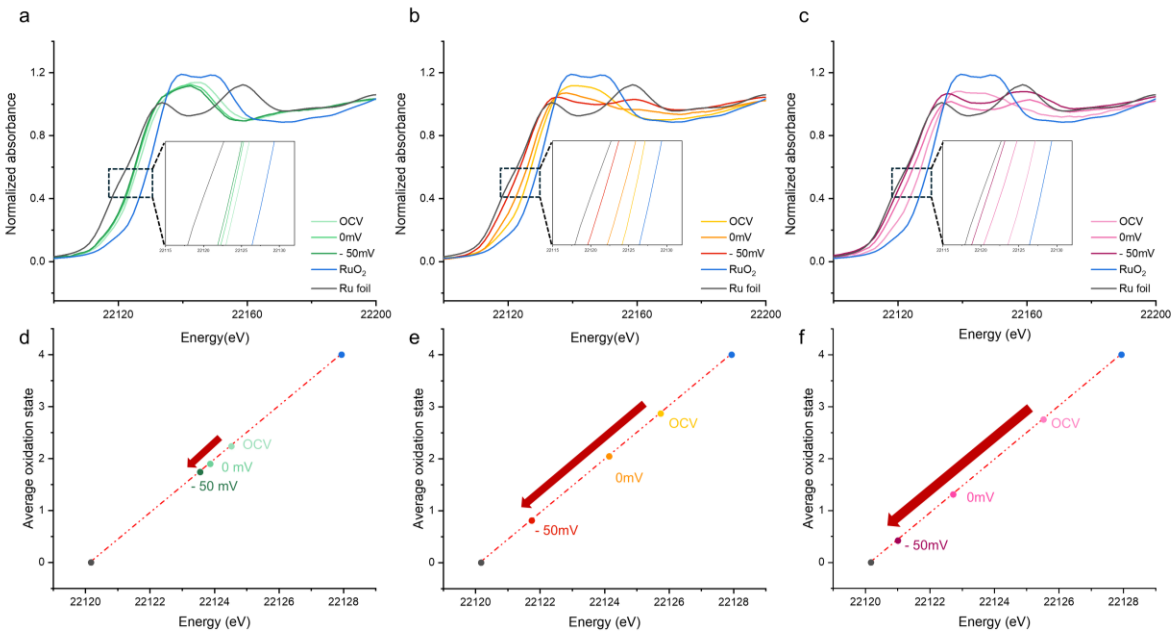

Fig. S29 In situ Ru K-edge XANES spectra and average Ru oxidation states. The spectra were recorded at open circuit voltage (OCV) and applied potentials of 0 mV and - 50 mV (vs. RHE) for (a) Ru/NKB-200, (b) Ru/NKB-500, and (c) Ru/NKB-800. Ru foil and RuO_2 are plotted as references, and the insets display magnified views of the absorption edge shifts. Corresponding average Ru oxidation states derived from edge position for (d) Ru/NKB-200, (e) Ru/NKB-500, and (f) Ru/NKB-800.

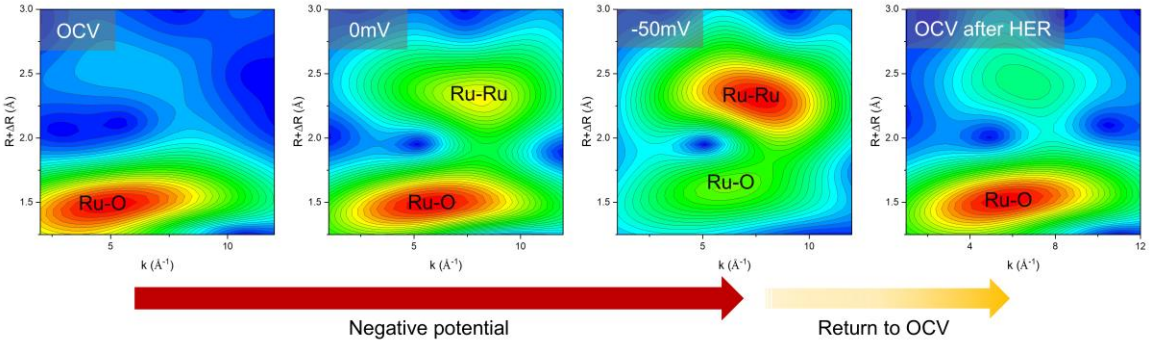

Fig. S30 In situ Ru K-edge WT-EXAFS contour plots of Ru/NKB-500 recorded at OCV, and applied potentials of 0 mV and - 50 mV (vs. RHE), and OCV after HER.

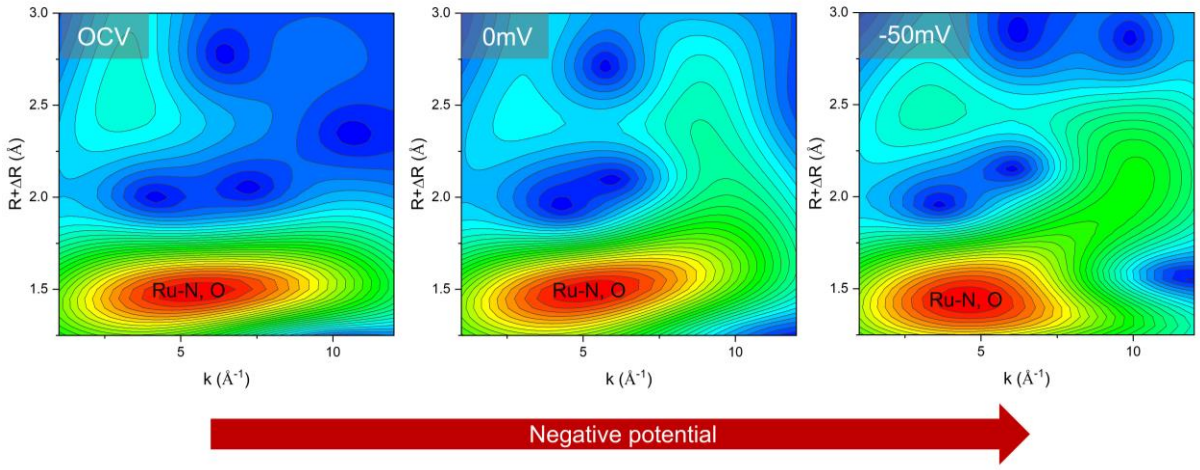

Fig. S31 In situ Ru K-edge WT-EXAFS contour plots of Ru/NKB-200 recorded at OCV, and applied potentials of 0 mV and - 50 mV (vs. RHE).

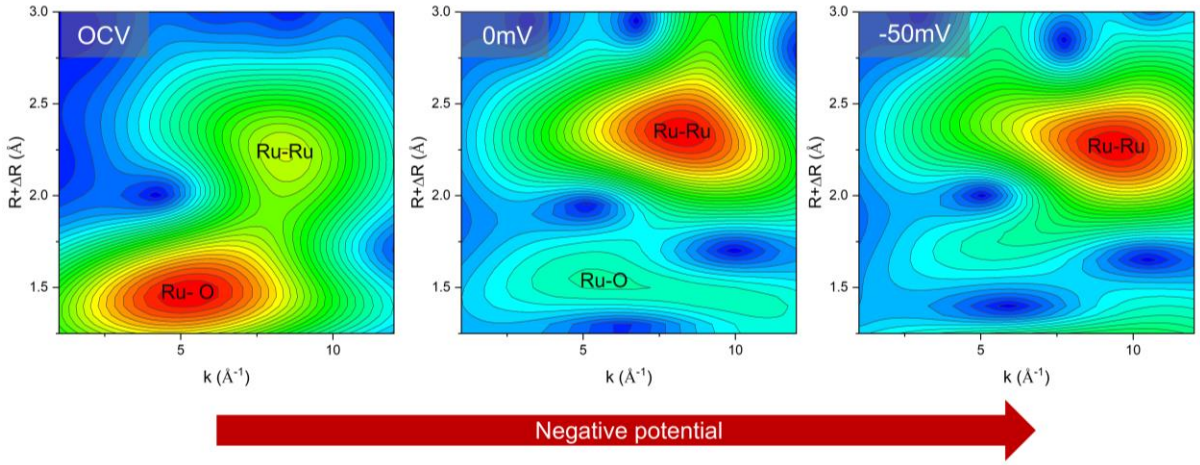

Fig. S32 In situ Ru K-edge WT-EXAFS contour plots of Ru/NKB-800 recorded at OCV, and applied potentials of 0 mV and - 50 mV (vs. RHE).

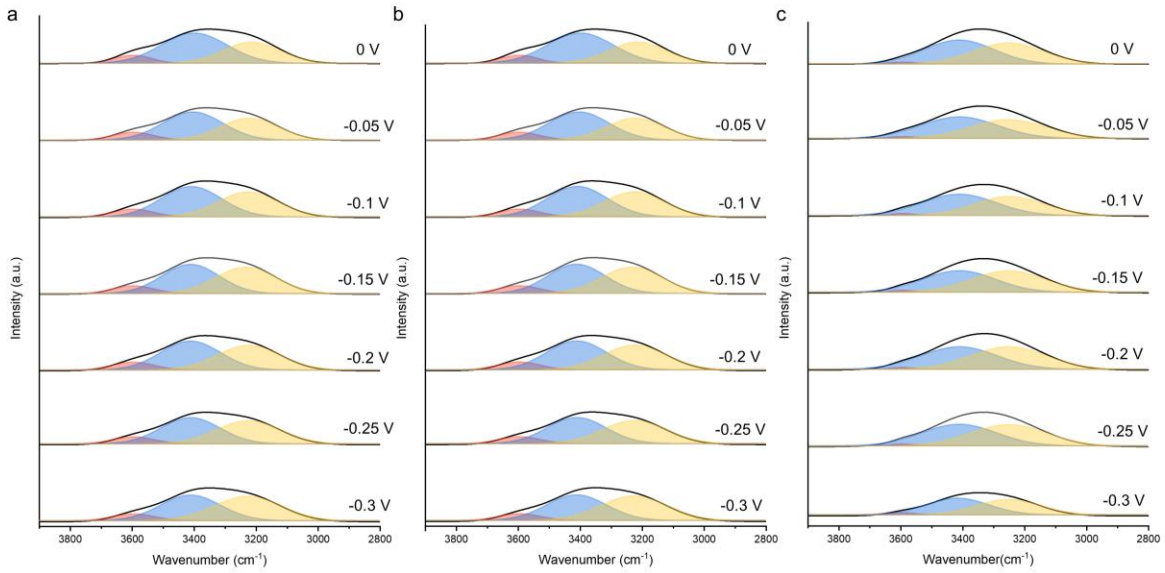

Fig. S33 In situ electrochemical ATR-SEIRAS spectra in the O-H stretching region (3800-2800 cm^{-1}). The spectra were recorded in 1.0 M KOH under applied potentials from 0 to - 0.3 V (vs. RHE) for (a) Ru/NKB-200, (b) Ru/NKB-500, and (c) Ru/NKB-800. The colored shaded areas represent the deconvoluted components of interfacial water molecules. (red: gap H_2O, blue: above-gap H_2O, yellow $K^+ \cdot H_2O$).

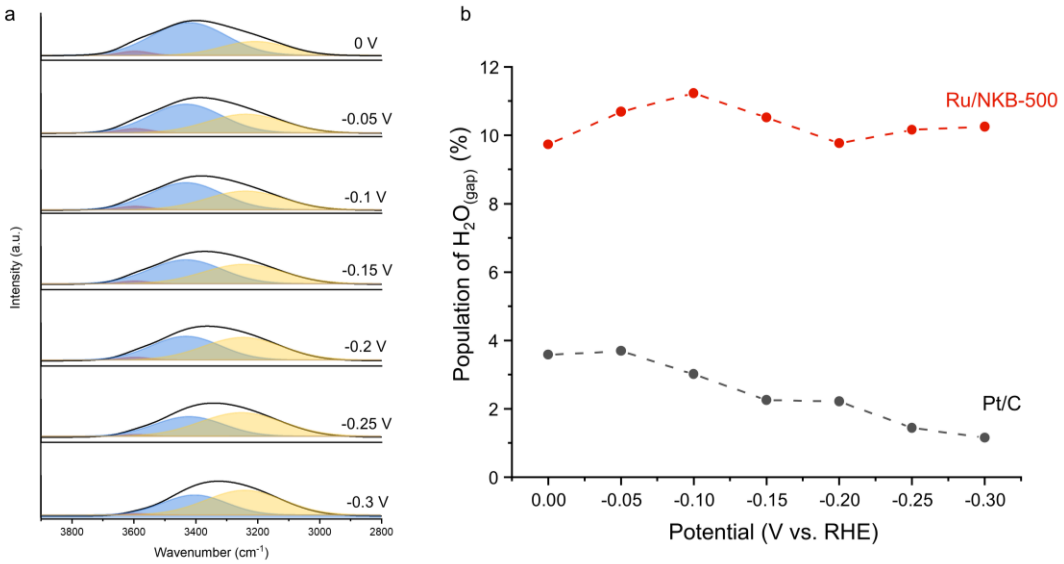

Fig. S34 In situ ATR-SEIRAS spectra in the O-H stretching region (3800-2800 cm^{-1}) recorded in 1.0 M KOH under applied potentials from 0 to - 0.3 V vs. RHE. (a) Deconvoluted O-H stretching bands of Pt/C. Colored shaded areas represent the deconvoluted components of interfacial water molecules. (red: gap H_2O blue: above-gap H_2O, yellow $K^+ \cdot H_2O$). (b) Potential-dependent comparison of the relative proportion of gap H_2O for Ru/NKB-500 and Pt/C.

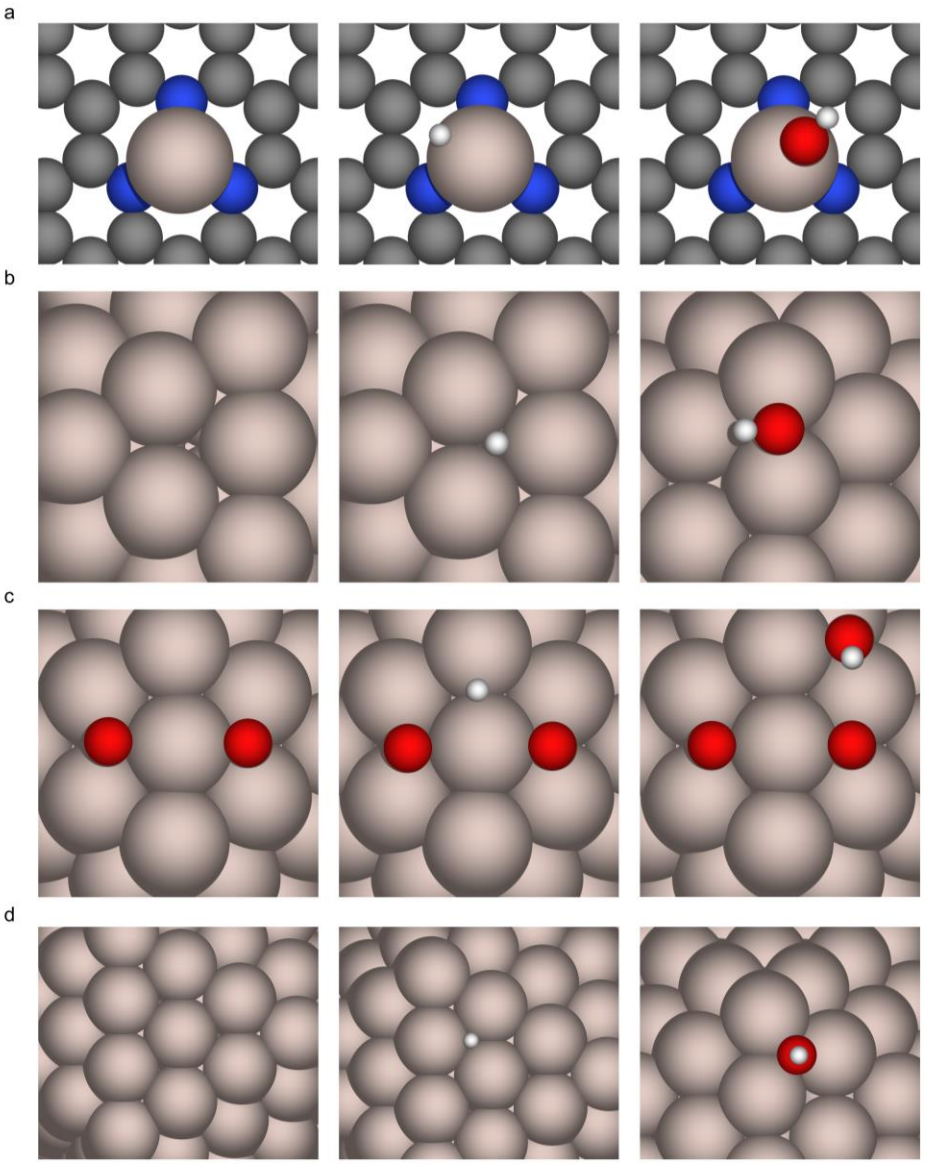

Fig. S35 Atomic models of Ru surfaces used for DFT calculations of H* and OH* adsorption. (a) Ru/NKB-200, (b) metallic and (c) oxidized surface models for Ru/NKB-500, and (d) Ru/NKB-800. For each row, the left, middle, and right panels correspond to the pristine surface model, the H*-adsorbed model, and the OH*-adsorbed model, respectively.

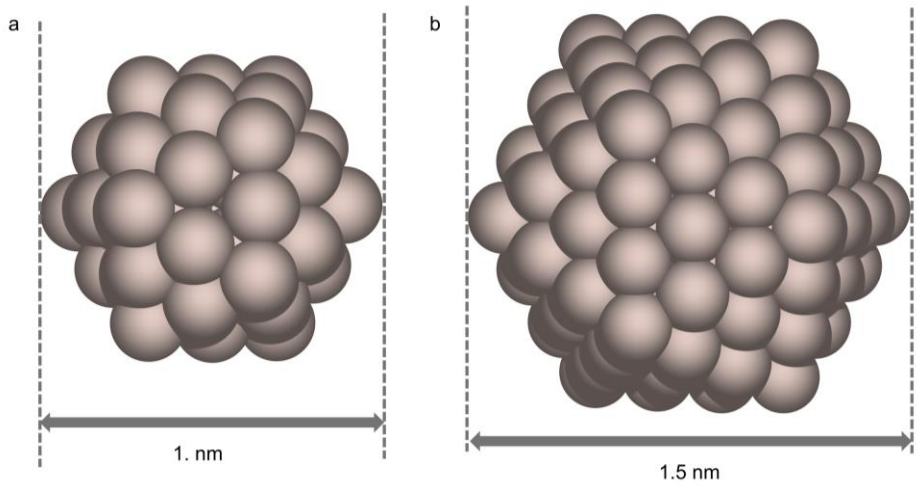

Fig. S36 Atomic models of Ru clusters used for DFT calculations. (a) Ru_{55} cluster model for Ru/NKB-500. (b) Ru_{147} cluster model for Ru/NKB-800.

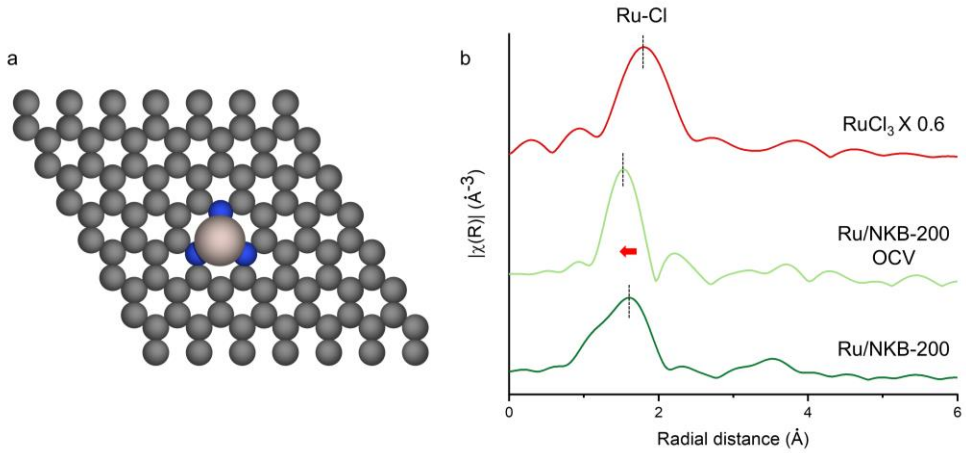

Fig. S37 Ru-N_3 coordination model for Ru/NKB-200 supported by in situ FT-EXAFS analysis. (a) Ru-N_3 model for Ru/NKB-200. (b) In situ FT-EXAFS spectra of Ru/NKB-200 compared with $RuCl_3$ reference, showing the disappearance of Ru-Cl coordination.

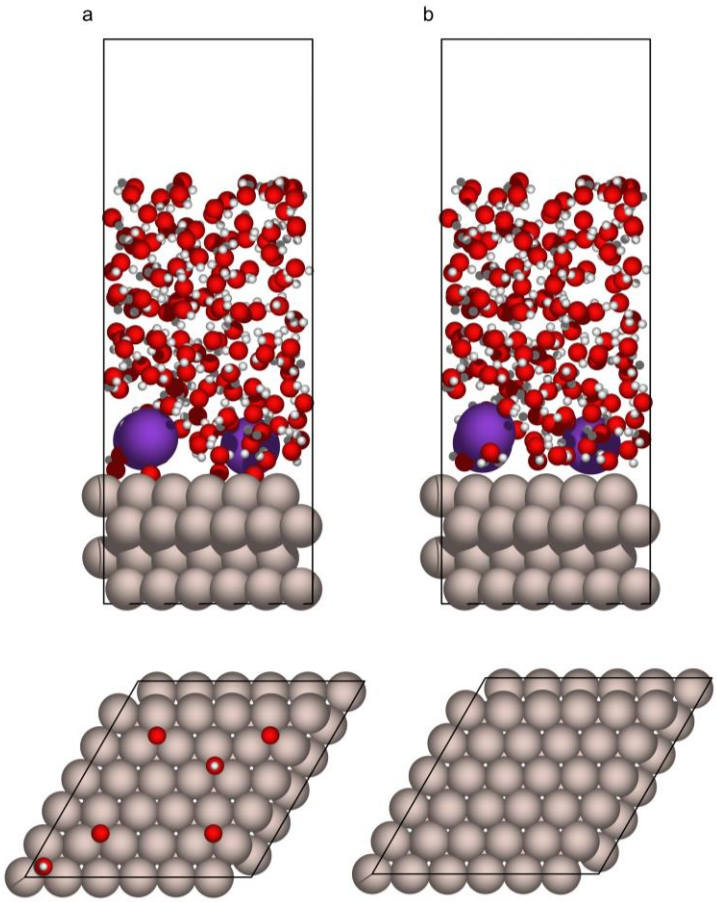

Fig. S38 Computational models and representative MD snapshots for interfacial water simulations. Representative MD snapshots of interfacial water structure (top) and the corresponding structural surface models (bottom) for (a) oxidized Ru (0001) slab, and (b) metallic Ru (0001) slab.

Supplementary Tables

Table S1. Ru metal contents (wt%) of Ru/NKB-T catalysts measured by ICP-MS.

Catalysts	Ru/NKB-200	Ru/NKB-350	Ru/NKB-500	Ru/NKB-650	Ru/NKB-800
NM contents (wt%)	2.67	2.77	2.95	3.18	3.38

Table S2. LCF results derived from Ru K-edge XANES spectra for Ru/NKB-T catalysts (T = 200, 350, 500, 650 and 800 ℃). The average Ru oxidation state was calculated by assigning oxidation states of 0 and + 4 to Ru foil and RuO_2, respectively.

Sample	Fraction of Ru (%)	Fraction of RuO_2 (%)	Average oxidation state	Reduced χ^2
Ru/NKB-200	55.9	44.1	1.76	0.00373
Ru/NKB-350	29.4	70.6	2.82	0.00117
Ru/NKB-500	25.3	74.7	2.99	0.00042
Ru/NKB-650	42.3	57.7	2.3	0.00115
Ru/NKB-800	62	38	1.52	0.00057

Table S3. Structural parameters derived from Ru K-edge EXAFS fitting results for Ru/NKB-T catalysts and reference standards. CN: coordination number, R: interatomic distance, and σ^2: Debye-Waller factor. The goodness of fit is represented by R-factor (weighting: k^2)

Sample	Shell	CN	R (Å)	σ^2 (10^{-3} Å^2)	R-factor
Ru	Ru-Ru (1)	6	2.64	2.1	0.0079
	Ru-Ru (2)	6	2.71	2.1	
RuO_2	Ru-O (1)	1.93	1.94	0.93	0.020
	Ru-O (2)	3.86	1.99		
	Ru-O-Ru (1)	2.07	3.14		
	Ru-O-Ru (2)	4.16	3.32		
	Ru-O-Ru (3)	6.62	3.58		
Ru/NKB-800	Ru-O	3.59	1.97	9.10	0.008
	Ru-Ru	4.13	2.66	5.88	
	Ru-O-Ru	0.88	3.13		
Ru/NKB-650	Ru-O	3.61	1.98	5.13	0.012
	Ru-Ru	3.77	2.69	16.8	
	Ru-O-Ru	1.19	3.13		
Ru/NKB-500	Ru-O	4.34	1.99	7.22	0.007
	Ru-Ru	2.9	2.70	23.88	
	Ru-O-Ru	1.31	3.13	13.04	
Ru/NKB-350	Ru-O	2.51	1.98	0.80	0.015
	Ru-Cl	0.50	2.32		
	Ru-Ru	1.89	2.70	18.79	
	Ru-O-Ru	0.84	3.13		
Ru/NKB-200	Ru-N	2.82	2.12	11.23	0.019
	Ru-Cl	1.44	2.30	11.57	
	Ru-Ru	0.75	2.62		

Table S4. Comparison of alkaline HER performances of Ru/NKB-500 with other recently reported Ru-based electrocatalysts on 1.0 M KOH condition. The comparison parameters included NM mass loading, overpotential at - 10 mA cm^{-2} and Tafel slope**.**

Catalyst	NM Loading (μg_{NM} cm^{-2})	η_{10} (mV)	Tafel slope (mV dec^{-1})	*References*
Ru/NKB-500	15	20	30	This work
Pt/C	15	71	105	This work
Ru/C	15	39	62	This work
Pt/C (42 μg cm^{-2})	42	40	86	This work
1.38nm Ru NP	7	32	29	ACS Catal., 13, 13638-13649 (2023)
Ru_3Ni-N-C	31	8	35	Energy Environ. Sci., 18, 6273-6282 (2025)
Ru-YNC	4.75	22	39	Energy Environ. Sci., 18, 6141-6153 (2025)
Ru_{NPs}-$RuCr_{APs}$-N-C	3	31	53	Adv. Mater., 37, 2419360 (2025)
Mn-RuO_2	200	16	25	Adv. Energy. Mater, 2500815 (2025)
Ru_1/PNC	13	16	39.4	J. Am. Chem. Soc., 147, 3874-3884 (2025)
HTS-Ru-NCs/TiN	40	16.3	36	Adv. Mater., 36, 2403525 (2024)
$NiFeRu_{SA+NP}$-DOBDC	24	25	39.1	Adv. Energy Mater., 15, 2404714 (2025)
Ru/Mo_2C/MoO_2	36	19	18.3	Adv. Mater., 36, 2410039 (2024)
$Ru_{SA/NP}$-PNCFs	35	8	21.7	Joule, 8, 1790-1803 (2024)
Ru_1-Mo_2C	34	10.8	38.5	Energy Environ. Sci., 17, 1397-1406 (2024)
$Co_{SA}Ru_{AC}$@NCB	400	8	20.7	Nat. Commun., 15, 8216 (2024)
Ru/NC-10	160	15.8	34.6	Adv. Sci., 12, 2414012 (2025)
ac-$Ce_{SA}RuO_x$	68	8.3	23.1	Adv. Mater., 37, e08893 (2025)
Ru@PRC	36	28	27.9	Angew. Chem. Int. Ed., 63, e202411125 (2024)

Table S5. Comparison of average market prices of Ruthenium and Platinum in recent 3 months from various sources. All prices are converted to USD g^{-1}.

Source	Ruthenium (USD g^{-1})	Platinum (USD g^{-1})	Price Ratio (Ru/Pt)
Umicore Precious Metals Managements	33.274	59.862	0.555
Johnson Matthey PGM management	30.380	55.146	0.550
Heraeus Precious Metals	29.257	53.946	0.542
Average	30.970	56.318	0.550

Table S6. Comparison of AEMWE performance for Ru/NKB-500 and other recently reported Ru-based cathode catalysts in cells utilizing commercial membranes.

Membrane electrode assembly (MEA)			Temperature (℃)	Current density		Mass activity ($A\ mg_{NM}^{-1}$ @1.8V)	Price activity ($A\ dollar^{-1}$ @1.8V)	References
Cathode ($mg_{NM}\ cm^{-2}$)	Membrane	Anode ($mg_{NM}\ cm^{-2}$)		1.8V ($A\ cm^{-2}$)	2V ($A\ cm^{-2}$)			
Ru/NKB-500 (0.15)	X37-50 Grade RT	NiFe alloy	50	2.41	5.34	16.1	518.6	This work
Ru/NKB-500 (0.03)	X37-50 Grade RT	NiFe alloy	50	1.94	4.14	64.67	2088	This work
Ru/NKB-500 (0.125)	PiperION	NiFe alloy	80	3.19	7.19	25.52	824	This work
Pt/C (0.15)	X37-50 Grade RT	NiFe alloy	50	1.19	2.15	7.9	140.3	This work
PtRu/C (0.15)	X37-50 Grade RT	NiFe alloy	50	1.59	2.98	10.6	221.4	This work
Pt-Ru/RuO_2 (0.47)	AEMION™	NiFe LDH	55	0.45	1.7	1.1	59.5	Nat. Commun., 15, 1447 (2024)
Ru/NC-10 (0.4)	FAA-3-PK-130	NiFe LDH	70	0.72	1.08	1.8	58.1	Adv. Sci., 12, 2414012 (2025)
Ru-YNC (0.019)	X37-50	NiFe-LDH	80	0.72	-	37.89	1223.6	Energy Environ. Sci., 18, 6141-6153 (2025)
Ru_3Ni-N-C (0.29)	-	NiFe LDH	80	1.49	2.38	5.14	165.97	Energy Environ. Sci., 18, 6273-6282 (2025)
CS-Ru-40 (0.65)	PiperION	IrO_2 (2)	60	1.64	3.35	0.62	4.87	Energy Environ. Sci., 18, 2243-2253 (2025)
Ru-NPs/WC_x (0.043)	PiperION	NiFe LDH	80	1.42	2.84	33.02	1066	Nat. Commun.,16, 10617 (2025)
Mn-RuO_2 (0.12)	FAA-3-PK-130	NiFe LDH	85	0.64	-	5.36	357.33	Adv. Energy Mater., 2500815 (2025)
Ru NC/RuSA-N_2O_2 (0.08)	W-25	NiFe LDH	80	2.73	-	34.13	1102	Adv. Energy Mater., 15, 2501331 (2025)
RuNd-NMC (0.1)	PiperION	IrO_2 (-)	60	1.34	1.85	-	-	Adv. Energy Mater., 15, e04124 (2025)
$Ru_{CS/SA}$/α-MoC_{1-x}/C	X37-50	RuO_2	60	1.73	-	-	-	Adv. Mater., 38, e19840 (2025)
La_1-Ru_n/NC (0.03)	FAA-3-PK-130	Ni Foam	80	2.42	5.57	80.67	2604.7	Energy Environ. Sci., 18, 4302-4311 (2025)
Ni-RuO_2	PiperION	RuO_2	60	1.48	3.26	-	-	Angew. Chem. Int. Ed., 64, e202421869 (2025)
$Li_{3.0}RuSn_{0.8}$NWs/C (0.1)	PiperION	$NiFeO_xH_y$/NF	80	1.92	5.53	19.2	620	J. Am. Chem. Soc., 147, 7711-7720 (2025)
Ru_1/PNC (0.1)	FAA-3-50	$IrRuO_x$ (-)	60	0.74	1.42	-	-	J. Am. Chem. Soc., 147, 3874-3884 (2025)
HTS-Ru-NCs/TiN (0.32)	FAA-3-50	$NiFeO_x$	60	1.82	-	5.68	183.4	Adv. Mater., 36, 240325 (2024)
Ru_1-Mo_2C (0.013)	X37-50	NiFe LDH	65	0.89	1.8	68.3	2205.4	Energy Environ. Sci., 17, 1397-1406 (2024)
UP-$RuNi_{SAs}$/C	-	NiFe LDH	70	0.92	-	-	-	Nat. Commun., 15, 2218 (2024)
$Ru_{8\%}$-Co_3O_4	FAA-3-PK-130	$Ru_{8\%}$-Co_3O_4	85	0.43	0.84	-	-	Adv Energy Mater., 15, 2500700 (2025)
Ru/Mo_2C/MoO_2	PiperION	IrO_2	60	0.09	0.34	-	-	Adv. Mater., 36, 2410039 (2024)
Ru/Ti_4O_7 (0.4196)	PiperION	Ru/Ti_4O_7 (0.4196)	80	0.47	1.58	0.56	18	Nat. Commun., 15, 2728 (2024)

Membrane electrode assembly (MEA)			Temperature (℃)	Current density		Mass activity (A mg_{NM}^{-1} @1.8V)	Price activity (A $dollar^{-1}$ @1.8V)	References
Cathode (mg_{NM} cm^{-2})	Membrane	Anode (mg_{NM} cm^{-2})		1.8V (A cm^{-2})	2V (A cm^{-2})			
Ru/NKB-500 (0.15)	X37-50 Grade RT	NiFe alloy	50	2.41	5.34	16.1	518.6	This work
Ru/NKB-500 (0.03)	X37-50 Grade RT	NiFe alloy	50	1.94	4.14	64.67	2088	This work
Ru/NKB-500 (0.125)	PiperION	NiFe alloy	80	3.19	7.19	25.52	824	This work
NA-RuNi/C	X37-50	NA-RuNi/C	60	0.49	0.94	-	-	Energy Environ. Sci., 16, 285-294 (2023)
Ru/Zn-N-C (0.00639)	FAA3-PK-130	NiFe	60	1.06	3.3	165.8	5353.6	Adv. Mater., 36, 2308798 (2024)
MnRu/C60-3 (0.6006)	PiperION	NiFe	60	1.12	-	1.86	60.2	Adv. Funct. Mater., 34, 240906 (2024)
Ru/P-MoB (0.11)	X37-50	RuO_2	60	1.14	-	10.4	335.8	Adv. Energy. Mater., 14, 2303384 (2024)
Ru SAs/WC_x (0.032)	X37-50 Grade 60	$NiFeOH_x$	80	1.04	1.74	32.5	1049.4	J. Am. Chem. Soc., 146, 4883-4891 (2024)

Table S7. LCF results derived from in situ Ru K-edge XANES spectra for Ru/NKB-T catalysts (T = 200, 500 and 800 °C). The average Ru oxidation state was calculated by assigning oxidation states of 0 and + 4 to Ru foil and RuO_2, respectively.

Sample	Fraction of Ru (%)	Fraction of RuO_2 (%)	Average oxidation state	Reduced χ^2
Ru/NKB-500 (OCV)	29.7	70.3	2.81	0.00121
Ru/NKB-500 (0 mV)	55	45	1.8	0.00145
Ru/NKB-500 (- 10 mV)	66.1	33.9	1.36	0.00183
Ru/NKB-500 (- 20 mV)	71.1	28.9	1.16	0.00092
Ru/NKB-500 (- 50 mV)	81.5	18.5	0.74	0.00092
Ru/NKB-500 (- 100mV)	83.6	16.4	0.66	0.00097
Ru/NKB-200 (OCV)	39.7	60.3	2.41	0.00272
Ru/NKB-200 (0 mV)	49.4	50.6	2.02	0.00434
Ru/NKB-200 (- 50 mV)	54.3	45.7	1.83	0.00476
Ru/NKB-800 (OCV)	38.4	61.6	2.46	0.00067
Ru/NKB-800 (- 0 mV)	75.7	24.3	0.97	0.00089
Ru/NKB-800 (- 50 mV)	87.8	12.2	0.49	0.00102

1. B. Liu, H. Yao, W. Song, L. Jin, I. M. Mosa, J. F. Rusling, S. L. Suib and J. He, *J. Am. Chem. Soc.*, 2016, **138**, 4718–4721.
2. H. Funke, A. C. Scheinost and M. Chukalina, *Phys. Rev. B*, 2005, **71**, 094110.
3. C. A. Campos-Roldán, R. G. González-Huerta and N. Alonso-Vante, *J. Electrochem. Soc.*, 2018, **165**, J3001–J3007.
4. D. Li, E. J. Park, W. Zhu, Q. Shi, Y. Zhou, H. Tian, Y. Lin, A. Serov, B. Zulevi, E. D. Baca, C. Fujimoto, H. T. Chung and Y. S. Kim, *Nat. Energy*, 2020, **5**, 378–385.
5. H. Miyake, S. Ye and M. Osawa, *Electrochem. Commun.*, 2002, **4**, 973–977.
6. G. Kresse and J. Hafner, *Phys. Rev. B*, 1993, **47**, 558–561.
7. G. Kresse and J. Furthmüller, *Phys. Rev. B*, 1996, **54**, 11169–11186.
8. P. E. Blöchl, *Phys. Rev. B*, 1994, **50**, 17953–17979.
9. J. P. Perdew, K. Burke and M. Ernzerhof, *Phys. Rev. Lett.*, 1996, **77**, 3865–3868.
10. J. K. Nørskov, J. Rossmeisl, A. Logadottir, L. Lindqvist, J. R. Kitchin, T. Bligaard and H. Jónsson, *J. Phys. Chem. B*, 2004, **108**, 17886–17892.
11. S. Batzner, A. Musaelian, L. Sun, M. Geiger, J. P. Mailoa, M. Kornbluth, N. Molinari, T. E. Smidt and B. Kozinsky, *Nat. Commun.*, 2022, **13**, 2453.
12. M. L. D. Chuin Wei Tan, Mit Kotak, Gabriel de Miranda Nascimento, Seán R. Kavanagh, Laura Zichi, Menghang Wang, Aadit Saluja, Yizhong R. Hu, Tess Smidt, Anders Johansson, William C. Witt, Boris Kozinsky, Albert Musaelian, *arXiv*, 2025, **2504**, 16068.
13. N. Michaud-Agrawal, E. J. Denning, T. B. Woolf and O. Beckstein, *J. Comput. Chem.*, 2011, **32**, 2319–2327.
14. J. Wang, C. S. Hsu, T. S. Wu, T. S. Chan, N. T. Suen, J. F. Lee and H. M. Chen, *Nat. Commun.*, 2023, **14**, 6576.